nature chemical biology

ARTICLES

https://doi.org/10.1038/s41589-021-00852-0

Check for updates

ATP-competitive partial antagonists of the IRE1α RNase segregate outputs of the UPR

Hannah C. Feldman[1], Rajarshi Ghosh[2,3,4,5,6], Vincent C. Auyeung[2,3,4,5,6], James L. Mueller[2,7], Jae-Hong Kim[2,3,4,5,6], Zachary E. Potter[1], Venkata N. Vidadala[1], B. Gayani K. Perera[1], Alina Olivier[2,3,4,5,6], Bradley J. Backes[2,3], Julie Zikherman[2,7], Feroz R. Papa[2,3,4,5,6] ✉ and Dustin J. Maly[1,8] ✉

The unfolded protein response (UPR) homeostatically matches endoplasmic reticulum (ER) protein-folding capacity to cellular secretory needs. However, under high or chronic ER stress, the UPR triggers apoptosis. This cell fate dichotomy is promoted by differential activation of the ER transmembrane kinase/endoribonuclease (RNase) IRE1α. We previously found that the RNase of IRE1α can be either fully activated or inactivated by ATP-competitive kinase inhibitors. Here we developed kinase inhibitors, partial antagonists of IRE1α RNase (PAIRs), that partially antagonize the IRE1α RNase at full occupancy. Biochemical and structural studies show that PAIRs promote partial RNase antagonism by intermediately displacing the helix αC in the IRE1α kinase domain. In insulin-producing β-cells, PAIRs permit adaptive splicing of *Xbp1* mRNA while quelling destructive ER mRNA endonucleolytic decay and apoptosis. By preserving *Xbp1* mRNA splicing, PAIRs allow B cells to differentiate into immunoglobulin-producing plasma cells. Thus, an intermediate RNase-inhibitory 'sweet spot', achieved by PAIR-bound IRE1α, captures a desirable conformation for drugging this master UPR sensor/effector.

Overwhelming the protein-folding and structural maturation capacity of the early secretory pathway leads to accumulation of misfolded and immature secretory proteins in the ER[1]. Eukaryotic cells evolved intracellular signaling pathways to respond to such 'ER stress'. These UPR pathways maintain cellular secretory function and physiological health in the face of remediable ER stress[2]. First discovered in unicellular eukaryotes, UPR pathways promote homeostatic/adaptive outputs through transcriptional upregulation of ER protein-folding and quality control factors that extract terminally misfolded proteins back to the cytosol for degradation[3,4]. However, in mammalian cells experiencing irremediable ER stress levels that cannot be mitigated by these adaptive arms, the UPR triggers programmed cell death, typically through mitochondrial apoptosis[2]. Multicellular organisms likely benefit from culling irreversibly ER-stressed cells because of the potential harm caused by secreting misfolded protein cargo. However, in chronic states of such 'terminal' UPR activation, the cumulative decrement of cell numbers through unchecked programmed cell death may actively promote cell degenerative diseases[5].

One critical life–death switch in the UPR is governed by the ER transmembrane multidomain sensor protein IRE1α[6]. IRE1α is activated following ER stress elevation, causing this sensor to self-associate in the ER membrane. This event causes cytosolic kinase domain of IRE1α to *trans*-autophosphorylate, which results in subsequent activation of its C-terminal endoribonuclease (RNase) catalytic domain[7–9]. The range of available IRE1α RNase activation states runs a gamut from the inactive to the active and the hyperactive, with the level of activity controlled by the proximal kinase module. Low-level activation of the IRE1α kinase/RNase promotes cleavage of the adaptive XBP1 transcription factor mRNA to initiate its frame-shift splicing, while high-level kinase/RNase hyperactivation expands the RNase substrate repertoire to myriad ER-localized mRNAs that become endonucleolytically cleaved in a process termed regulated IRE1α-dependent decay (RIDD), thus initiating apoptosis[6,10–12].

For maintaining cellular homeostasis, a priori, the sweet spot for IRE1α RNase activation may lie at a level at which adaptive *Xbp1* mRNA splicing remains permissible but without the initiation of RIDD. The cellular effects of such a metastable activation state have been demonstrated with IRE1α mutants (some found naturally as somatic mutations in cancers that act as RNase hypomorphs) and chemical genetic systems[6,10]. Although ATP-competitive inhibitors can control endogenous IRE1α RNase activity through the kinase domain, such allosteric modulators have largely been shown to enforce opposite extremes of activation states[13–16]. Therefore, an optimal mode of engaging the endogenous IRE1α ATP-binding site has hitherto not been achieved.

Here, we demonstrate that it is possible to design ATP-competitive inhibitors, which we named PAIRs, that fully engage the IRE1α kinase domain but only partially inhibit its RNase activity. By performing systematic structure–activity analyses of ATP-competitive inhibitors, we identified the chemical features that distinguish PAIRs from previously reported allosteric activators and full inhibitors of IRE1α. Through comparisons of inhibitor-bound IRE1α complexes, we find that the partial antagonism of PAIRs is a result of their ability to only intermediately displace helix αC outward in

[1]Department of Chemistry, University of Washington, Seattle, WA, USA. [2]Department of Medicine, University of California, San Francisco, San Francisco, CA, USA. [3]Lung Biology Center, University of California, San Francisco, San Francisco, CA, USA. [4]Department of Pathology, University of California, San Francisco, San Francisco, CA, USA. [5]Diabetes Center, University of California, San Francisco, San Francisco, CA, USA. [6]Quantitative Biosciences Institute (QBI), University of California, San Francisco, San Francisco, CA, USA. [7]Division of Rheumatology, Rosalind Russell and Ephraim P. Engleman Arthritis Research Center, University of California, San Francisco, San Francisco, CA, USA. [8]Department of Biochemistry, University of Washington, Seattle, WA, USA. ✉e-mail: feroz.papa@ucsf.edu; djmaly@uw.edu

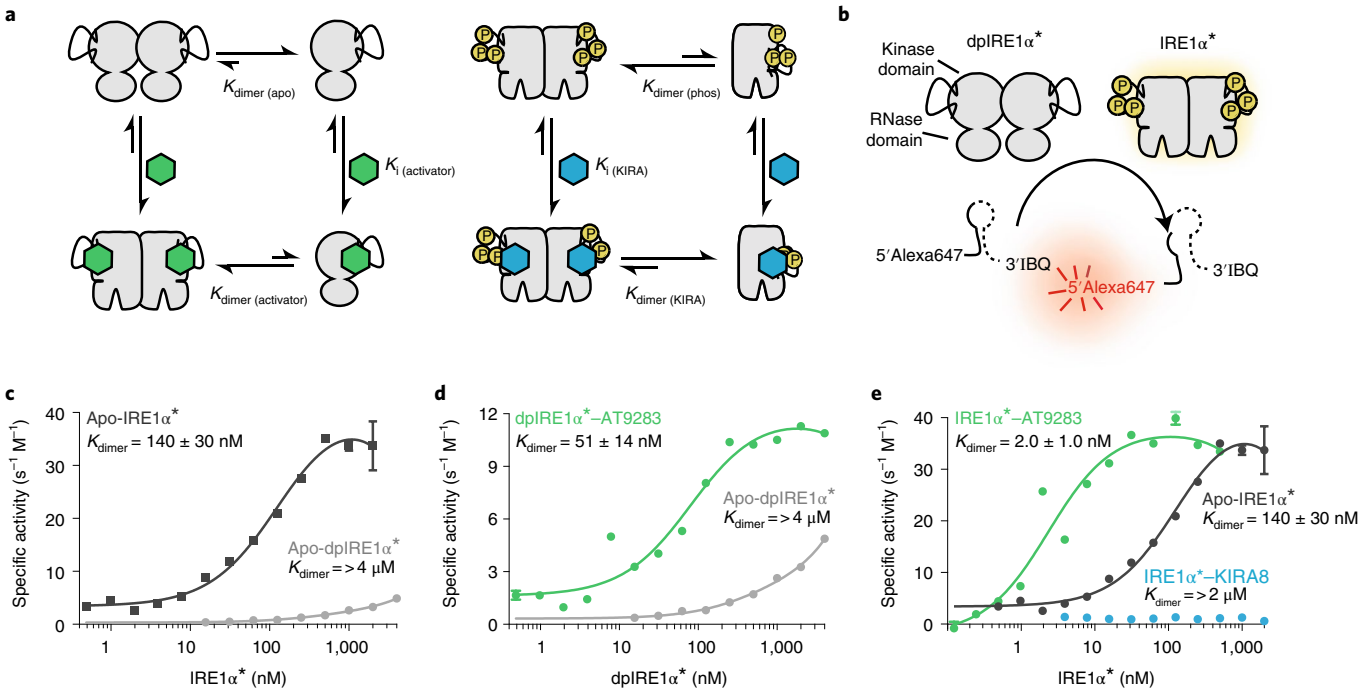

Fig. 1 | IRE1α dimerization is modulated by ATP-binding site occupancy. a, Model of how ATP-competitive inhibitors affect the oligomerization state of different phosphorylation states of IRE1α. K_i denotes inhibition constant. **b**, Schematic of the recombinant constructs IRE1α* and dpIRE1α* (top), which consist of the cytosolic kinase and RNase domains of IRE1α, and the in vitro XBP1 minisubstrate cleavage assay (bottom); IBQ, Iowa Black Quencher. **c**, Dimerization affinity (K_{dimer}) curves for apo-IRE1α* (dark gray) and apo-dpIRE1α* (light gray). Data points shown are the mean of $n = 3$ independent experiments ± s.e.m. **d**, K_{dimer} curve for the dpIRE1α*–AT9283 complex (green). Data points shown are the mean of $n = 3$ independent experiments ± s.e.m. The K_{dimer} curve of apo-dpIRE1α* (light gray) from **c** is shown for comparison. **e**, K_{dimer} curves for the IRE1α*–AT9283 (green) and IRE1α*–KIRA8 (blue) complexes. Data points displayed are shown as the mean of $n = 3$ independent experiments ± s.e.m. The K_{dimer} curve of apo-IRE1α* (dark gray) from **c** is shown for comparison.

the IRE1α kinase domain from an active conformation. We further show that enforcing such an optimal IRE1α inhibitory state in cells allows partial antagonism of the RNase, sufficient to permit adaptive *Xbp1* mRNA splicing while mostly inhibiting RIDD. Finally, we show that PAIRs have the unique ability to segregate distinct biological outputs of IRE1α in cellular systems by chiseling away destructive (RIDD-dependent) cell fate outcomes from adaptive (XBP1 splicing-dependent) ones. Thus, PAIRs may represent a new pharmacological modality for addressing ER stress-induced cell degeneration by preserving an adaptive UPR while blunting terminal UPR outputs.

Results

ATP-competitive ligands tune IRE1α dimerization affinity. To better understand how to achieve an optimal RNase-inhibitory state, we established an in vitro framework for quantitatively characterizing how kinase domain ATP-binding site occupancy affects the RNase activity of IRE1α. Formation of a 'back-to-back' dimer characterized by an extensive interface between the kinase and RNase domains of each IRE1α protomer is required for the IRE1α RNase domain to be catalytically active (Fig. 1a)[17,18]. Phosphorylation of the IRE1α kinase activation loop stimulates RNase activity by promoting dimer formation[14,19]. Furthermore, ligands that occupy the ATP-binding site of the kinase domain can also stimulate the RNase activity of IRE1α by promoting dimer formation[18,20]. We measured the ability of a purified kinase/RNase domain construct of IRE1α, IRE1α*, to cleave a fluorogenic XBP1 RNA minisubstrate as a function of IRE1α* concentration to quantitatively determine the dimerization affinity (K_{dimer}) of IRE1α (Fig. 1b). Using this assay, we found that IRE1α*, which is basally autophosphorylated on its activation loop, demonstrated a K_{dimer} in the high nanomolar range (Fig. 1c). A quantitatively dephosphorylated IRE1α* construct (dpIRE1α*) (Supplementary Fig. 1) was also capable of forming RNase-active dimers but with a much lower dimerization affinity ($K_{dimer} > 4\,\mu M$), showing that activation loop phosphorylation dramatically strengthens back-to-back dimer formation.

ATP-competitive ligands that allosterically promote IRE1α RNase activity also increase the dimerization affinity of the kinase/RNase domains of IRE1α. We found that the K_{dimer} of dpIRE1α* was ~80-fold lower when its kinase domain was complexed to the ATP-competitive ligands AT9283 or AZD7762 (Fig. 1d and Supplementary Fig. 2). AT9283 and AZD7762 also led to a similar fold increase in the dimerization affinity of IRE1α*, demonstrating that ATP-competitive ligands further promote dimer formation of activation loop-phosphorylated IRE1α (Fig. 1e and Supplementary Fig. 3).

Next, we tested how a class of ATP-competitive ligands, called kinase inhibiting RNase attenuators ('KIRAs'), that inactivate the IRE1α RNase activity through the kinase domain affect dimerization affinity[13]. We found that IRE1α* was unable to form RNase-active dimers at any concentration tested when bound to the high-affinity ligand KIRA8 (**1**) (ref. [21]) or even to a lower-affinity KIRA (**2**) (Fig. 1e and Extended Data Fig. 1). Thus, it appears that KIRAs stabilize an ATP-binding site conformation that almost completely disrupts the ability of IRE1α to form an RNase-active back-to-back dimer. This result is consistent with our observation that full-length IRE1α-mediated splicing of *Xbp1* mRNA was almost completely suppressed in ER-stressed insulinoma (INS-1) cells treated with KIRA8 (Extended Data Fig. 2), despite the accumulation of unfolded proteins that promote lumenal domain

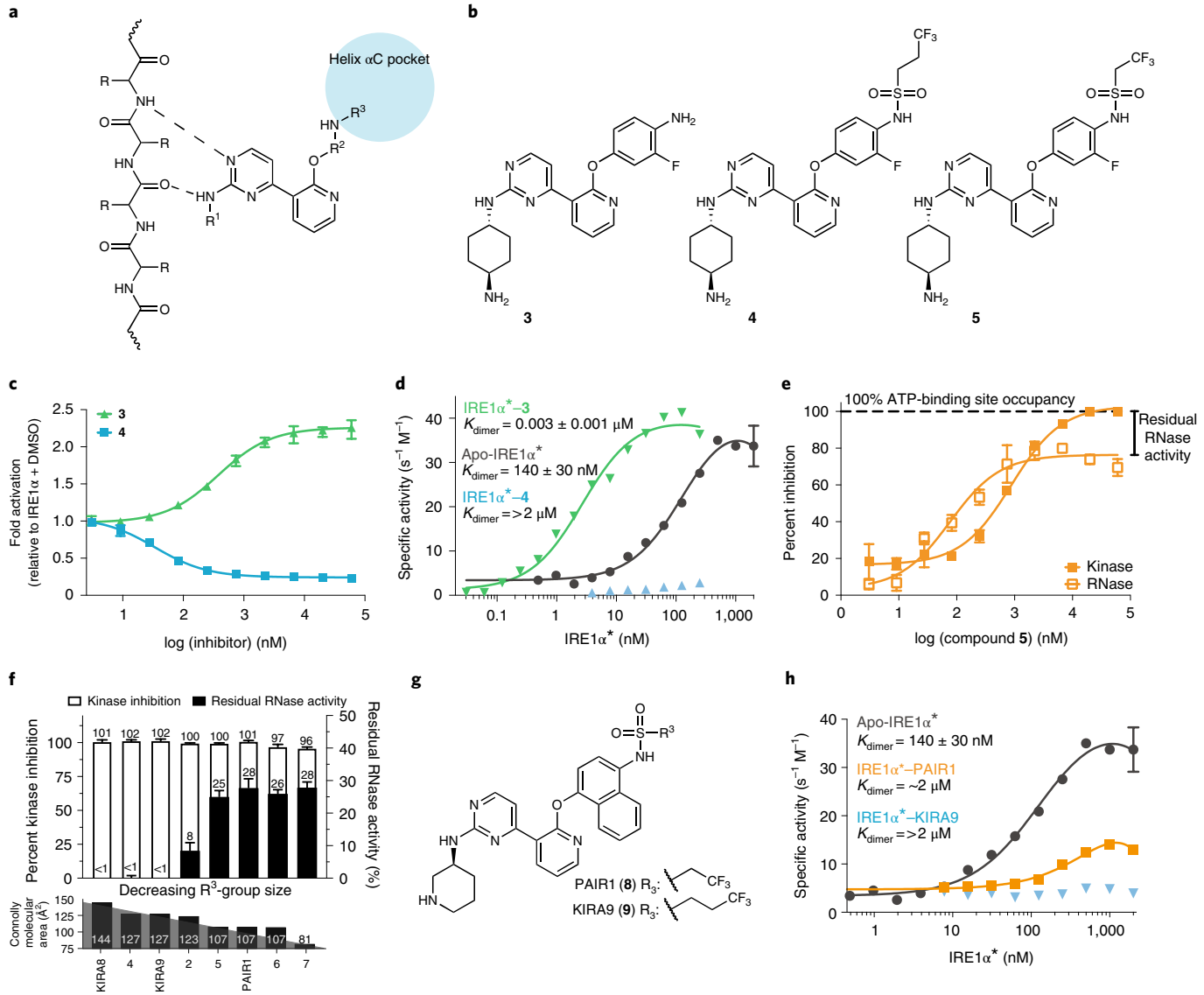

Fig. 2 | Partial antagonists of IRE1α RNase activity. a, Proposed binding mode of the pyridine–pyrimidine scaffold with the IRE1α ATP-binding site. Structural elements that are varied in our study are labeled as R^1, R^2 or R^3. **b**, Structures of compounds **3**–**5**. **c**, RNase activities of IRE1α* under varying concentrations of **3** and **4** relative to apo-IRE1α*. Data shown are the mean of $n = 3$ independent experiments ± s.e.m. **d**, K_{dimer} curves for the IRE1α*–**3** (green) and IRE1α*–**4** (blue) complexes. Values shown are means of $n = 3$ independent experiments ± s.e.m. The K_{dimer} curve of apo-IRE1α* (dark gray) from Fig. 1c is shown for comparison. **e**, The kinase and RNase activities of IRE1α* under varying concentrations of **5**. IRE1α* retains ~20% of its RNase activity (residual activity) at full ATP-binding site occupancy. Data shown are the mean of $n = 3$ independent experiments ± s.e.m. **f**, Three-way correlation of kinase inhibition (a proxy for ATP-binding site occupancy), residual RNase activity and R^3-group size measured as Connolly molecular surface area (Å^2). Kinase inhibition and residual RNase activity are shown as the mean of $n = 3$ independent experiments ± s.e.m. **g**, Structures of compounds PAIR1 and KIRA9. **h**, K_{dimer} curves for the IRE1α*–PAIR1 (orange) and IRE1α*–KIRA9 (blue) complexes. Values shown are the mean of $n = 3$ independent experiments ± s.e.m.

oligomerization. Thus, KIRA-bound IRE1α appears to be locked in an RNase-inactive monomeric state in vitro and in cells.

Partial antagonists of IRE1α RNase activity. We speculated that it should be possible to identify ATP-competitive ligands that only intermediately weaken the dimerization affinity of IRE1α and hence preserve some RNase outputs, unlike KIRAs that enforce a completely crippled RNase activity state. To better understand how to design such partial antagonists of IRE1α RNase activity, we explored ATP-competitive ligands based on the pyridine–pyrimidine scaffold of KIRA8 (Fig. 2a,b). The pyridine–pyrimidine scaffold of KIRA8 makes extensive contacts with the ATP-binding site of IRE1α that are distal to regions that undergo major conformational changes following dimerization, allowing for the introduction of substituents that have the potential to differentially modulate dimer affinity while maintaining reasonable potency. We first generated and tested compound **3**, which contains a *trans*-hexanediamine and a 4-amino-3-fluorophenol at the R^1 and R^2 positions, respectively, of the pyridine–pyrimidine scaffold. We found that **3** dose-dependently inhibited the kinase activity of IRE1α and activated its RNase activity (Fig. 2c and Supplementary Figs. 4a and 5). By contrast, we observed that compound **4** (Fig. 2b and Supplementary Fig. 4b), which contains a 3-trifluoropropylsulfonamide group at the R^3 position but is otherwise identical to **3**, dose-dependently inhibited the kinase and RNase activities of IRE1α* (Fig. 2c) and completely suppressed the formation of RNase-active dimers (Fig. 2d).

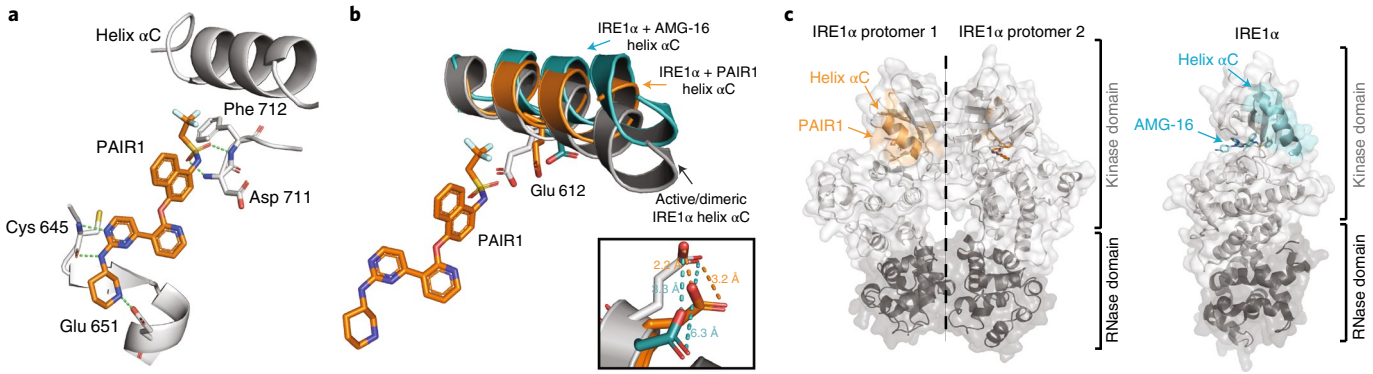

Fig. 3 | Cocrystal structure of the IRE1α–PAIR1 complex. a, Interactions of PAIR1 with the ATP-binding site of IRE1α. Key interactions (dashed green lines) between PAIR1 (orange sticks) and IRE1α are highlighted. Interacting residues are shown as gray sticks. **b**, Superimposition of the helix αCs of the IRE1α–PAIR1 (orange) and IRE1α–AMG-16 (teal; PDB: 4U6R) complexes and active IRE1α (gray). The inset displays the displacement of Glu 612 within the helix αC relative to active IRE1α* (gray; PDB: 5HGI). **c**, Global structure of the IRE1α–PAIR1 (left) and IRE1α–AMG-16 (right) complexes. PAIR1-bound IRE1α crystallizes as a back-to-back dimer (the twofold symmetry axis is denoted by a dashed line), while AMG-16-bound IRE1α crystallizes as a monomer. Each protomer contains a kinase domain (light gray) and an RNase domain (dark gray).

We reasoned that ATP-competitive ligands that are capable of partially antagonizing the RNase activity of IRE1α would likely contain R^3 substituents that are smaller than the 3-trifluoropropylsulfonamide group of **4** but larger than those of **3**. Indeed, we found that compound **5**, which contains a 2-trifluoroethylsulfonamide R^3 substituent (Fig. 2b), quantitatively inhibited the kinase activity of IRE1α* but only partially (~80%) inhibited its RNase activity (Fig. 2e). Thus, only a small difference in the size of the substituent at the R^3 position can lead to partial versus complete inhibition of the IRE1α* RNase activity. On the basis of this observation, we generated several additional ATP-competitive ligands (**6**, **7** and **8** (hereafter, **8** will be referred to as PAIR1); Extended Data Fig. 3a–c) that provided quantitative kinase activity inhibition but only partially inhibited the IRE1α RNase activity (Extended Data Fig. 4); we named these compounds PAIRs. To demonstrate that partial RNase inhibition was not contingent on the scaffold but rather the size of the R^3 substituent, we also generated compounds **9** (KIRA9) and **10**, which displayed quantitative inhibition of both the kinase and RNase domains of IRE1α (Fig. 2f,g and Extended Data Figs. 3d–f and 4b,c). As predicted, we found that this partial antagonism of RNase activity was a result of a weakened dimerization affinity rather than enforcement of a monomeric state (Fig. 2h and Supplementary Fig. 6). Thus, it was possible to design inhibitors that fully occupy the IRE1α ATP-binding site, yet only partially antagonize its RNase activity.

PAIRs stabilize a partially displaced helix αC. To provide mechanistic insight into the partial RNase antagonism of PAIRs, we obtained a 1.85-Å resolution cocrystal structure of PAIR1 bound to IRE1α*. As expected, PAIR1 occupies the ATP-binding site of IRE1α*, with the pyrimidine–pyridine scaffold forming two hydrogen-bonding interactions with the hinge region. Additional interactions include a hydrogen-bonding interaction between the naphthyl sulfonamide group and the backbone of the DFG-motif and a salt bridge between the piperidine substituent of PAIR1 and Glu 651 in the αH-helix (Fig. 3a and Supplementary Table 1). These aforementioned interactions are highly similar to those made between IRE1α* and the KIRAs AMG-16 (**11**) (Protein Data Bank (PDB): 4U6R) and KIRA8 (PDB: 6URC), which share the same pyrimidine–pyridine scaffold as PAIR1 (Supplementary Fig. 7).

We speculated that differences in how PAIRs and KIRAs influence the conformation of the helix αC could explain the variable effects that they have on dimerization affinity. Helix αC is a dynamic regulatory element that lines the IRE1α* ATP-binding pocket; when it is in the active conformation, it forms a significant portion of the RNase-active back-to-back dimer interface[14]. Consistent with the ability of PAIR1 to partially inhibit the IRE1α* RNase activity, helix αC of the PAIR1–IRE1α* complex is rotated and displaced from the active conformation (Supplementary Fig. 8). Superimposition of the PAIR1–IRE1α* structure with IRE1α* bound to the KIRA AMG-16, which also presents its R^3 sulfonamide from position 4 of a 4-amino-1-naphthol ether R^2 group, shows that the more compact 2-trifluoroethanesulfonamide R^3 substituent of PAIR1 leads to a smaller displacement of the helix αC from the active conformation than a 2-chlorophenylsulfonamide (Fig. 3b and Extended Data Fig. 5). PAIR1 also leads to a smaller displacement of helix αC than KIRA8 (Extended Data Fig. 5c). Thus, the fact that PAIRs partially displace helix αC from an active conformation likely explains why they only reduce IRE1α*'s dimerization affinity.

The differences that we observe between PAIRs and KIRAs in their modulation of the dimerization affinity of IRE1α* in solution appear to be reflected in the oligomeric states of the PAIR1–IRE1α* and AMG-16–IRE1α* complexes in crystal structures[21]. We observed that PAIR1-bound IRE1α* crystallized as a back-to-back dimer, while the AMG-16-bound structure of IRE1α* was monomeric (Fig. 3c). However, the structure of the PAIR1–IRE1α* dimer is not identical to the RNase-active dimer. While a majority of the interface contacts that the RNase-active dimer forms are conserved in the PAIR1–IRE1α* structure, an interdimer salt bridge between Asp 620 and Arg 594/Arg 627, which was identified in a previous study as an essential interaction in IRE1α's formation of RNase-active dimers, is partially disrupted (Extended Data Fig. 6)[22]. Thus, PAIR binding leads to only a limited perturbation of the IRE1α* dimer interface, unlike KIRAs.

PAIR1 preserves XBP1 splicing but blocks RIDD. Before conducting cellular studies with PAIRs, we performed kinome selectivity profiling using a chemical proteomic method (Fig. 4a)[23–25]. Specifically, we measured the ability of **2**, **3**, **6**, **7**, PAIR1 and KIRA9 to compete with lysate kinases for binding to a nonselective kinase inhibitor matrix (kinobeads). Each compound (10 μM) was incubated with a standard kinobead matrix and a HEK293/HCT116 lysate mixture, and competed kinases were quantified. We found that all four PAIRs displayed high selectivity for IRE1α, with only a few off-target kinases observed (Fig. 4a and Supplementary Figs. 9 and 10). We selected PAIR1 for further studies because of its high selectivity for IRE1α and the availability of a KIRA (KIRA9) that only differs by one methylene group with equivalent potency and selectivity.

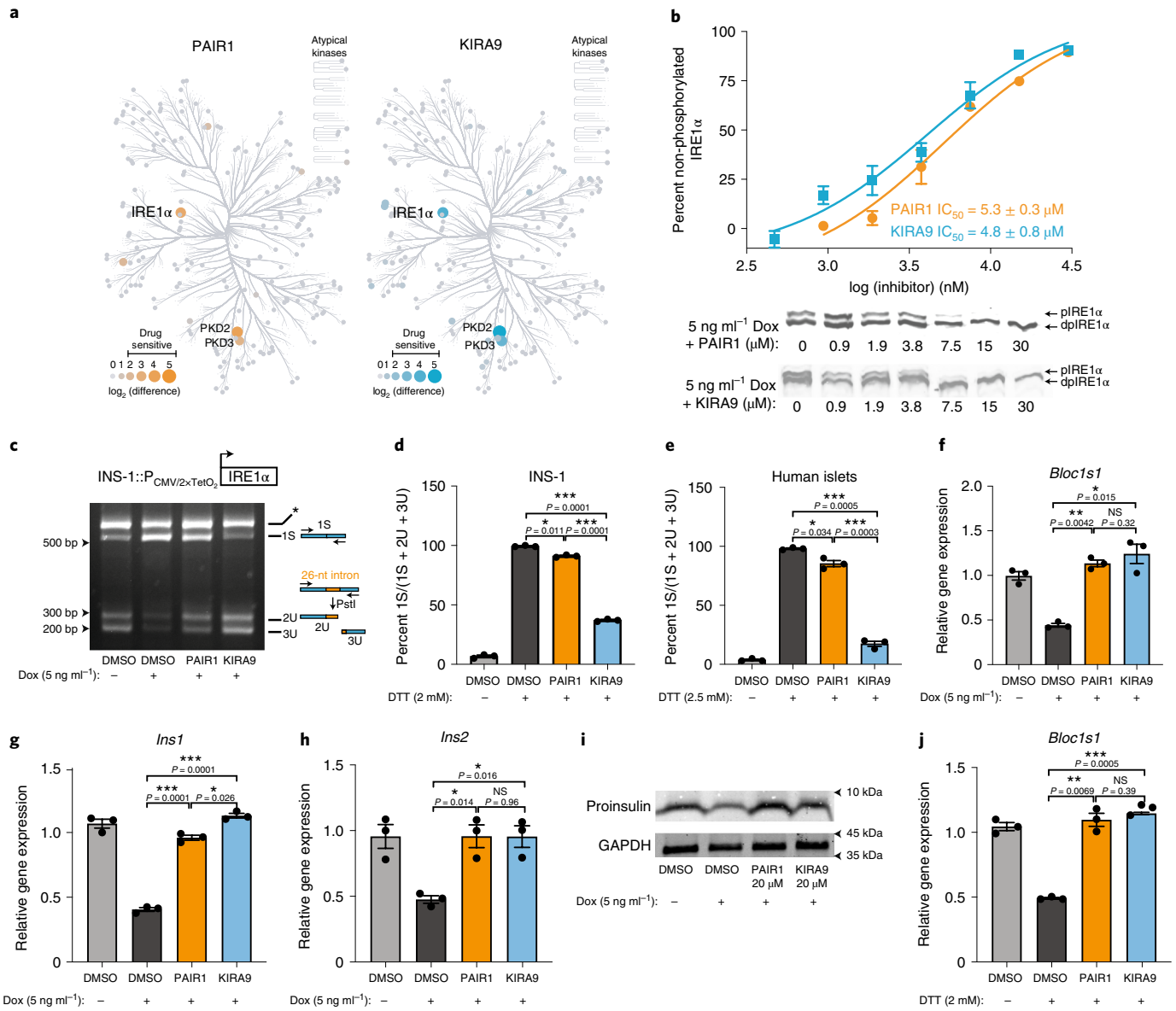

Fig. 4 | PAIR1 spares XBP1 splicing but blocks RIDD outputs in cells. a, Kinome selectivity of PAIR1 and KIRA9 determined by kinobead profiling. Identified kinases are shown with gray circles. Circle size and color are scaled to the $\log_2$ ratio (difference in label-free quantitation (LFQ) intensity) between DMSO and treatment with 10 μM of PAIR1 or KIRA9 (mean of $n = 4$). Kinases reported as drug sensitive ($\log_2$ (difference) > 2) were required to show significance from a two-sample *t*-test with a false discovery rate (FDR) *P* value of 0.05; PKD2/3, protein kinase D2/3. **b**, Immunoblots for total IRE1α from INS-1 cells expressing transgenic IRE1α under Dox control (referred to as INS-1::PCMV/2xTetO$_2$ cells) and treated with various concentrations of PAIR1 or KIRA9 followed by the addition of 5 ng ml^{-1} Dox (bottom). Samples were subjected to phostag SDS–PAGE, and percent non-phosphorylated IRE1α was determined from the ratio of non-phosphorylated IRE1α relative to total IRE1α (top). Values shown are the mean of $n = 3$ biologically independent samples ± s.e.m.; IC_{50}, half-maximal inhibitory concentration; pIRE1α, phosphorylated IRE1α. **c**, Ethidium bromide-stained agarose gels of XBP1 cDNA amplicons from the cells described in **b** that were treated with DMSO, PAIR1 or KIRA9 followed by the addition of 5 ng ml^{-1} Dox for 4 h. The cDNA amplicon of unspliced *Xbp1* mRNA is cleaved at a PstI site within a 26-nt intron to generate 2U and 3U (unspliced) amplicons. IRE1α-mediated cleavage of the intron and religation removes the PstI site to generate the 1S (spliced) amplicon. Asterisk indicates a spliced/unspliced XBP1 hybrid amplicon. bp, base pairs; nt, nucleotide. **d**,**e**, Percent spliced XBP1 (quantified from PstI-digested XBP1 cDNA amplicons) from parent INS-1 cells (**d**) or human islets (**e**) treated with DMSO, PAIR1 (20 μM) or KIRA9 (20 μM) followed by the addition of 1,4-dithiothreitol (DTT). Data shown are the mean of $n = 3$ biologically independent samples ± s.e.m. **f**–**h**, Quantitative real-time PCR (qPCR) of relative *Bloc1s1* (**f**), *Ins1* (**g**) and *Ins2* (**h**) mRNA levels from the cells described in **b** treated with DMSO, PAIR1 (20 μM) or KIRA9 (20 μM) followed by the addition of 5 ng ml^{-1} Dox. Data shown are the mean of $n = 3$ biologically independent samples ± s.e.m.; NS, not significant. **i**, Immunoblots for proinsulin from the cells described in **b** treated with DMSO, PAIR1 (20 μM) or KIRA9 (20 μM) followed by the addition of 5 ng ml^{-1} Dox for 72 h. GAPDH is shown as a loading control. **j**, qPCR of relative *Bloc1s1* mRNA levels from parent INS-1 cells treated with DMSO, PAIR1 (20 μM) or KIRA9 (20 μM) followed by the addition of DTT. Data shown are the mean of $n = 3$ biologically independent samples ± s.e.m. *P* values were calculated using two-tailed Student's *t*-test; $^*P < 0.05$, $^{**}P < 0.01$ and $^{***}P < 0.001$.

We next tested PAIR1 and KIRA9 in an INS-1 insulinoma stable cell line where IRE1α activation can be achieved through doxycycline (Dox)-inducible overexpression of a mouse IRE1α transgene[6]. We have previously demonstrated that this maneuver causes IRE1α to spontaneously self-associate and autophosphorylate, triggering RIDD and subsequently causing entry into mitochondrial apoptosis

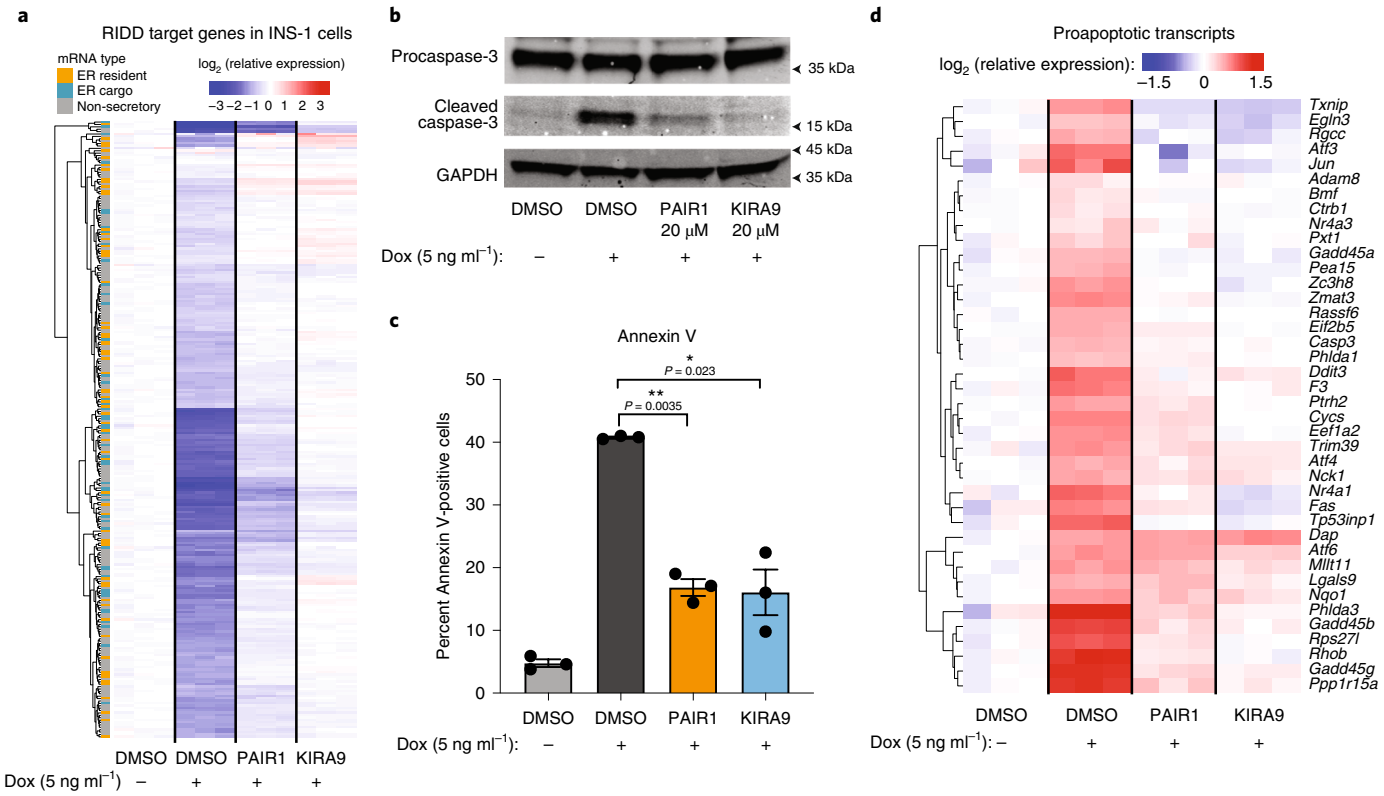

Fig. 5 | PAIR1 inhibits IRE1α-dependent mRNA decay and apoptosis. a, Hierarchical analysis of gene expression changes from RNA-seq profiling for INS-1 cells expressing IRE1α under Dox control and treated with DMSO, PAIR1 (20 μM) or KIRA9 (20 μM) followed by the addition of 5 ng ml^{-1} Dox for 24 h. Each column represents one biologically independent sample, with $n = 3$ samples per condition. **b**, Immunoblot of procaspase-3 and its cleavage product for cells subjected to the conditions described in Fig. 4i. GAPDH is shown as a loading control. **c**, Quantification of annexin V staining for the cells described in Fig. 4b that were treated with DMSO, PAIR1 (20 μM) or KIRA9 (20 μM) followed by the addition of 5 ng ml^{-1} Dox for 72 h. Data shown are the mean of $n = 3$ biologically independent samples ± s.e.m. *P* values were calculated using two-tailed Student's *t*-test; $^{*}P < 0.05$, $^{**}P < 0.01$ and $^{***}P < 0.001$. **d**, Hierarchical analysis of proapoptotic gene expression changes from the RNA-seq profiling described in **a**.

without the use of pleiotropic ER stress-inducing agents. Using phostag acrylamide gels, we found that both PAIR1 and KIRA9 were able to equivalently block the autophosphorylation induced by conditional overexpression of IRE1α in these lines at almost identical concentrations (Fig. 4b). Thus, PAIR1 and KIRA9 were able to fully engage the ATP-binding site of full-length, cellular IRE1α at comparable levels.

In contrast to KIRA9, we observed that PAIR1 largely preserved *Xbp1* mRNA splicing and expression of the frame-shifted XBP1s transcription factor protein in these cellular systems, despite equivalent kinase domain engagement at the concentration tested (Fig. 4c and Supplementary Fig. 11). Likewise, PAIR1 only weakly inhibited *Xbp1* mRNA splicing in INS-1 cells and human islets subjected to ER stress-inducing agents (Fig. 4d,e and Extended Data Fig. 7). However, consistent with the notion that downstream RIDD should be equivalently blunted by PAIRs and KIRAs, we found that the RIDD substrates *Bloc1s1* and the mRNAs encoding proinsulin (*Ins1* and *Ins2* in rodents) were rescued by both PAIR1 and KIRA9 (Fig. 4f–h)[10]. The recovery of *Ins1*/*Ins2* mRNA led to increased levels of proinsulin protein (Fig. 4i). Likewise, both PAIR1 and KIRA9 were also able to equivalently blunt RIDD in ER-stressed INS-1 cells (Fig. 4j).

PAIRs and KIRAs block ER-localized mRNA decay and apoptosis. Next, to systematically compare the transcriptomic effects of PAIR1 and KIRA9, we profiled INS-1 cells that conditionally overexpress IRE1α by RNA sequencing (RNA-seq). As above (Fig. 4), cells were treated with either DMSO or equivalent concentrations of PAIR1 or KIRA9, and IRE1α overexpression was induced with Dox. Total RNA was submitted for sequencing across entire transcripts. We observed that Dox treatment led to a >tenfold induction of the mouse *Ern1* transgene (Supplementary Fig. 12), and the dense coverage across the *Xbp1* locus enabled quantification of XBP1 splicing based on the reduced density of reads mapping to the noncanonical *Xbp1* intron. Consistent with measurements of XBP1 splicing by isoform-specific PCR (Fig. 4c), overexpression-induced *Xbp1* mRNA splicing was preserved in both DMSO- and PAIR1-treated cells but was blocked in KIRA9-treated cells at 4 h (Supplementary Fig. 13). At 24 h, when *Xbp1* mRNA splicing is saturated, splicing levels were still partially decreased in KIRA9-treated cells, yet were preserved in the presence of PAIR1 (Supplementary Fig. 13).

We next interrogated RIDD target gene expression in these cells (Fig. 5a). Previously, we showed that overexpression of IRE1α induced the endonucleolytic degradation of a population of mRNAs enriched for those predicted to be ER localized, such as those encoding ER-resident or ER cargo proteins (that is, 'secretome'), as occurs naturally during ER stress regimens[6]. We were able to recapitulate the 'RIDD signature' we defined previously in this model. Furthermore, downregulation of RIDD signature genes was antagonized by both PAIR1 and KIRA9 to a similar degree (Fig. 5a). Indeed, secretome transcripts were globally decreased by IRE1α overexpression compared to controls[26]. This effect was blocked by both PAIR1 and KIRA9 (Supplementary Fig. 14), consistent with a model whereby IRE1α docks to the translocon and, following hyperactivation and oligomerization, degrades nearby mRNAs being translated on ER membrane-associated ribosomes during the

process of cotranslational translocation of the nascent, emerging polypeptides (encoded by these ER-localized mRNAs) while they are being synthesized[27].

A priori, if *Xbp1* mRNA splicing inhibition is irrelevant for entry of cells into apoptosis, while RIDD promotes apoptosis, then both PAIR1 and KIRA9 should perform equivalently to each other in cytoprotection assays because they share the common feature that they cause equivalent rescue of RIDD. Consistent with this notion, we observed that both PAIR1 and KIRA9 markedly reduced the generation of cleaved caspase-3 and showed significant and similar cytoprotective efficacy in a mitochondrial apoptosis assay (annexin V positivity) (Fig. 5b,c). We previously showed that the RIDD activity of IRE1α promotes apoptosis by upregulating a pro-oxidant mediator and amplifier of terminal UPR signaling, thioredoxin-interacting protein (TXNIP), in INS-1 cells that overexpress IRE1α[10,28]. We found that TXNIP mRNA upregulation was blocked by both PAIR1 and KIRA9 (Fig. 5d, top). More generally, to the extent that proapoptotic genes (Gene Ontology (GO) term GO:0043065, positive regulation of apoptotic process) were upregulated by IRE1α overexpression, these changes were largely blunted to similar degrees by either PAIR1 or KIRA9 (Fig. 5d). Together, these results affirm that even though PAIRs only partially antagonize the IRE1α RNase (leaving *Xbp1* mRNA splicing extant), their ability to inhibit RIDD like KIRAs is fully sufficient to block the destructive effects of the terminal UPR leading to apoptosis.

PAIRs permit B cell differentiation into plasma cells. We next asked where should the effects of separating *Xbp1* mRNA splicing away from RIDD have discriminatory biological effects? We decided to interrogate the adaptive immune response to infection, through which naive B cells must undergo a complex maturation process, including radical expansion of the ER and associated protein-folding machinery, ultimately becoming plasma cells that are capable of secreting massive quantities of antibodies. As a master regulator of the UPR, IRE1α's initiation of XBP1 splicing is required for maturation of B cells into plasma cells in an adaptive UPR[29–31]. Because KIRAs and PAIRs have divergent effects on XBP1 splicing, we reasoned that they would have corresponding differential effects on plasma cell maturation. Before performing these experiments, we identified a more potent PAIR, PAIR2 (**12**), that could be used as a comparator to KIRA8 (Extended Data Fig. 8). PAIR2 demonstrated a similar ability to inhibit IRE1α's kinase activity as KIRA8 in vitro and in cells (Extended Data Fig. 8b,c). Pretreating INS-1 cells with PAIR2 before provision of KIRA8 (added at a concentration that led to significant inhibition of XBP1 splicing (Extended Data Fig. 8d)) prevented the KIRA8 inhibition of ER stress-induced XBP1 splicing (Extended Data Fig. 8e). Thus, PAIR2 is capable of completely occupying the IRE1α ATP-binding site in cells and can block the ability of a potent KIRA to inhibit XBP1 splicing. Furthermore, PAIR2 exhibited high selectivity in our kinome selectivity profiling assay (Extended Data Fig. 8f,g).

With two matched sets of PAIRs and KIRAs in hand, we next assessed how KIRA8, KIRA9, PAIR1 and PAIR2 affect the differentiation of lipopolysaccharide (LPS)-treated mouse splenocytes into antibody-secreting plasmablasts[32]. As expected, flow cytometric analysis showed that LPS treatment of B cells led to enhanced expression of intracellular XBP1s (Fig. 6a,b), a modest increase in live B cell numbers and dramatically increased plasma cell differentiation, as assessed by upregulation of CD138 expression and B220 downregulation relative to untreated splenocytes (Fig. 6c,d and Extended Data Figs. 9 and 10). LPS treatment also correspondingly increased plasma cell secretion of immunoglobulin M (IgM) into the culture medium (Fig. 6e,f). Splenocytes incubated with either KIRA8 or KIRA9 before LPS treatment showed reductions in XBP1s expression, plasma cell differentiation and IgM secretion in a dose-dependent manner that is in agreement with their relative in vitro potencies (Fig. 6a–f). By contrast, PAIR1 and PAIR2 were highly permissive for XBP1s expression, plasma cell differentiation and IgM secretion at all concentrations tested (Fig. 6a–f).

Finally, we confirmed that LPS treatment of splenocytes triggered elevations in XBP1 mRNA splicing, which were reversed with KIRA9 but not with PAIR1 (Supplementary Fig. 15a), as in the INS-1 and islet experiments shown previously. Like INS-1 cells and human islets treated with ER stress and in INS-1 cells overexpressing IRE1α, LPS treatment caused decay of *Bloc1s1* mRNA, which was rescued with either PAIR1 or KIRA9 (Supplementary Fig. 15b).

Discussion

In the unicellular eukaryote *Saccharomyces cerevisiae*, Ire1 initiates non-conventional splicing of the mRNA encoding the Hac1 transcription factor[33,34]; in another unicellular eukaryote, *Schizosaccharomyces pombe*, Ire1 exclusively promotes RIDD[35]. In both these model organisms, Ire1's enzymatic outputs physiologically restore ER secretory homeostasis during ER stress. In contrast to these unicellular eukaryotes, multicellular eukaryotes, especially mammals, have evolved an expanded number of UPR physiological outputs and other UPR sensor/effectors. Yet, the IRE1α ortholog in mammalian cells has preserved both non-conventional mRNA splicing of the mRNA encoding the XBP1 transcription factor and RIDD[6,12]. We first bifurcated these two outputs in mammalian cells through chemical genetics that enforce *Xbp1* mRNA splicing while averting RIDD through provision of the orthogonal kinase inhibitor 1NM-PP1 to drug-sensitized IRE1α mutants[6,10,36]. We also previously developed ATP-competitive ligands, which we named KIRAs, that fully antagonize the two RNase outputs of IRE1α at maximal occupancy.

Here, we developed ATP-competitive ligands, PAIRs, that partially antagonize endogenous IRE1α RNase activity at maximal occupancy of the kinase, which allows inhibition of RIDD while still preserving *Xbp1* mRNA splicing. Our biochemical and structural studies inform a cellular model wherein at maximal kinase occupancy the partial antagonism afforded by PAIRs allows for the preservation of dimeric IRE1α species that are sufficient for adaptive *Xbp1* mRNA splicing, while the higher-order oligomeric species needed for RIDD are prevented from forming (Supplementary Fig. 16a). By contrast, KIRA-bound IRE1α is monomerized at full kinase occupancy (Supplementary Fig. 16b); thus, at maximal occupancy, PAIRs have the ability to splay apart the inhibition of *Xbp1* mRNA splicing from the inhibition of RIDD, which KIRAs can only achieve at submaximal occupancy (Supplementary Fig. 16c).

We were able to achieve this partial antagonism by introducing substituents into PAIRs that only intermediately displace the helix αC of the IRE1α kinase domain from an active conformation. The helix αCs of protein kinases are dynamic structural features that are often allosterically coupled to distal binding interfaces[37,38]. In many cases, kinase helix αCs have been defined as two conformational extremes, an active 'in' form or an inactive 'out' conformation. PAIRs stabilize an intermediate conformational state between these two extremes, which appears to mimic unphosphorylated apo-IRE1α based on the similar K_{dimer} values of PAIR-bound IRE1α and unphosphorylated apo-IRE1α. As the helix αCs of many kinases are components of binding interfaces, it is likely that similar partial allosteric antagonism can be engineered into ATP-competitive inhibitors that target other kinases.

The 'Janus-like' nature of IRE1α's cytosolic RNase outputs is a challenge for the development of therapeutic modulators for treating diseases of ER stress-induced premature cell death. One RNase output, the cleavage of *Xbp1* mRNA, is critical to several adaptive responses to stress and cellular ontogenic processes[8,39,40]. The other RNase output, IRE1α-mediated RIDD, contributes to degenerative disease by promoting apoptosis in cells, including the β-islet cells

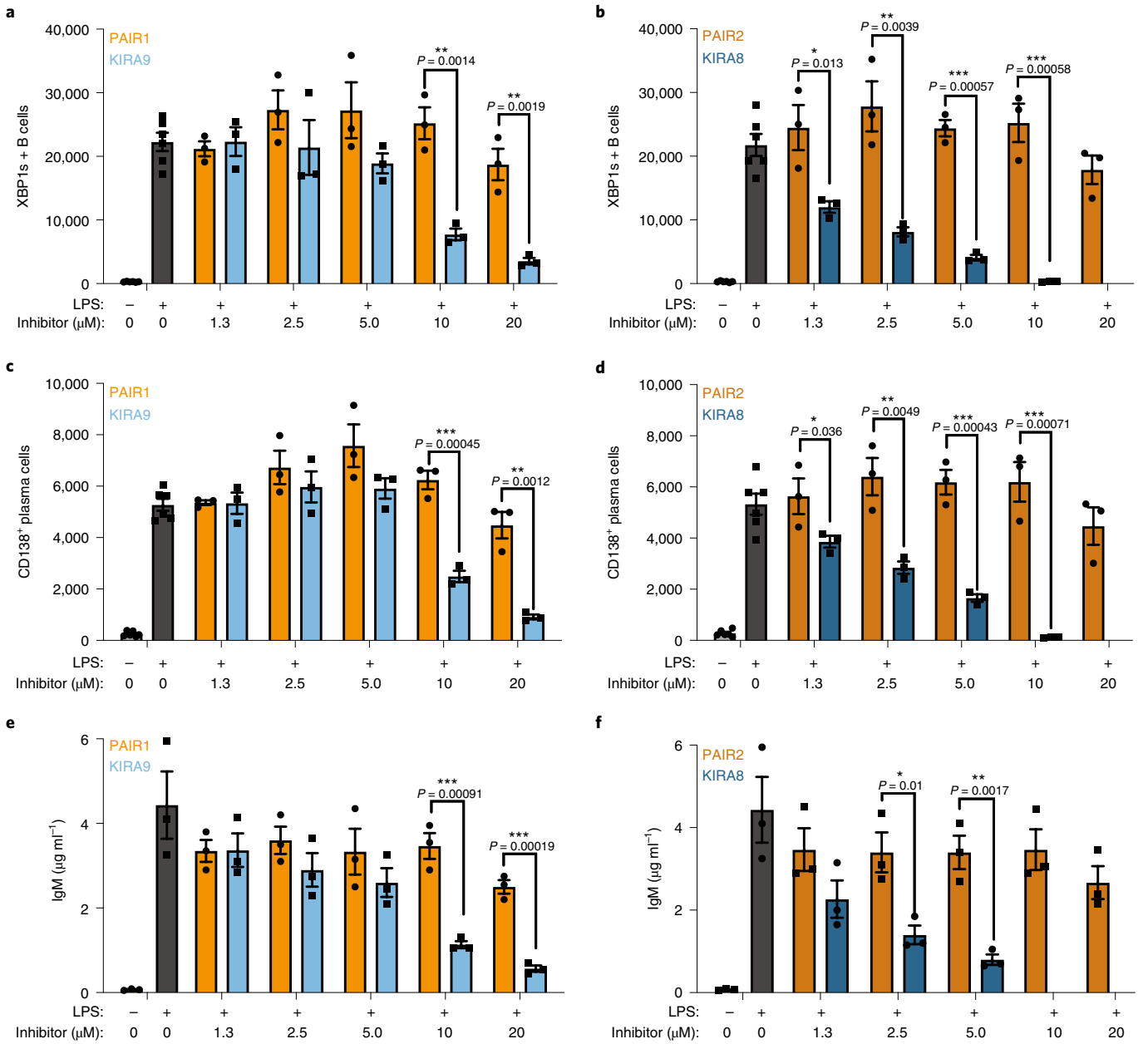

Fig. 6 | PAIRs and KIRAs differentially affect B cell differentiation. a,**b**, Quantification of XBP1s and B cells following treatment of mouse splenocytes with 1 μg ml^{-1} of LPS for 3 d in the presence or absence of various concentrations of PAIR1 (orange) or KIRA9 (teal) (**a**) or PAIR2 (dark orange) or KIRA8 (dark blue) (**b**). Quantification of CD138$^+$ cells following treatment of mouse splenocytes with 1 μg ml^{-1} LPS for 3 d in the presence or absence of various concentrations of PAIR1 (orange) or KIRA9 (teal) (**c**) or PAIR2 (dark orange) or KIRA8 (dark blue) (**d**). The gating scheme corresponding to **a**–**d** is shown in Extended Data Fig. 9. **e**, Enzyme-linked immunosorbent assay (ELISA) quantification of IgM secretion for the splenocytes treated as described in **a** and **c**. **f**, ELISA quantification of IgM secretion for the splenocytes treated as described in **b** and **d**. All data shown are the mean of $n = 3$ biologically independent samples ± s.e.m. *P* values were calculated using one-tailed Student's *t*-test; $^*P < 0.033$, $^{**}P < 0.002$ and $^{***}P < 0.001$. Data for 10 μM (**f**) and 20 μM (**b**,**d**,**f**) KIRA8 could not be generated due to cellular toxicity.

of the pancreas[6,12,41]. Before this work, small-molecule inhibitors of IRE1α's RNase blocked both of these outputs in tandem. PAIRs, therefore, represent a new modality for allosterically controlling IRE1α's RNase activity, stabilizing an intermediate conformational state that splits apart and segregates downstream RNase outputs.

Our newfound ability to bifurcate the RNase outputs of IRE1α with PAIRs creates the potential to drug the UPR in more nuanced ways than with existing modulators. We illustrated this by comparing the effect of a PAIR with a closely matched comparator KIRA in two distinct IRE1α-mediated cell fate regimens, one 'destructive' and the other 'constructive'. We predicted that if RIDD is necessary for apoptosis, then a KIRA and a PAIR would equivalently block RIDD and apoptosis. Indeed, this is what we found. The transcriptome of downregulated ER-localized mRNAs was largely superimposable between PAIR1 and KIRA9 treatment in INS-1 cells, as apoptotic gene upregulation was equivalently quelled by both inhibitors in this RIDD-driven physiological system. By comparison, in the 'constructive' model of de novo differentiation of B cells into immunoglobulin-producing plasma cells, we observed differential effects between PAIRs and KIRAs. By inhibiting *Xbp1* mRNA splicing (an event that is required

for building and expanding the ER physically and functionally during terminal differentiation), KIRAs demonstrated dose-dependent inhibitory effects on the production of CD138$^+$ plasma cells. However, PAIRs were largely permissive for plasma cell differentiation, even at maximal kinase occupancy, and retained *Xbp1* mRNA splicing. As in our β-cell models, reduction of *Bloc1s1* mRNA (a RIDD target) was rescued by both PAIRs and KIRAs.

Thus, we propose that the ability to segregate IRE1α's synthetic UPR outputs (that is, XBP1 transcription factor-driven) from its destructive RIDD outputs through applying PAIRs as comparators to monomerizing KIRAs has the broad potential to reveal the scope and diversity of distinct UPR biological outputs. Finally, we predict that PAIRs may be superior to existing IRE1α kinase (KIRAs) and other (direct) RNase inhibitors for treating diseases in which preservation of XBP1 splicing is important for optimal efficacy and safety[42–44]. In summary, the unique ability of PAIRs to preserve adaptive XBP1 splicing at full target engagement promises to provide new tools for studying the UPR and may represent a more desirable therapeutic modulation of IRE1α in myriad diseases caused by ER stress-induced premature cell death.

Online content

Any methods, additional references, Nature Research reporting summaries, source data, extended data, supplementary information, acknowledgements, peer review information; details of author contributions and competing interests; and statements of data and code availability are available at https://doi.org/10.1038/s41589-021-00852-0.

Received: 26 December 2020; Accepted: 1 July 2021;
Published online: 23 September 2021

References

1. Walter, P. & Ron, D. The unfolded protein response: from stress pathway to homeostatic regulation. *Science* **334**, 1081–1086 (2011).
2. Hetz, C. & Papa, F. R. The unfolded protein response and cell fate control. *Mol. Cell* **69**, 169–181 (2018).
3. Cox, J. S., Shamu, C. E. & Walter, P. Transcriptional induction of genes encoding endoplasmic reticulum resident proteins requires a transmembrane protein kinase. *Cell* **73**, 1197–1206 (1993).
4. Mori, K., Ma, W., Gething, M.-J. & Sambrook, J. A transmembrane protein with a cdc2+/CDC28-related kinase activity is required for signaling from the ER to the nucleus. *Cell* **74**, 743–756 (1993).
5. Oakes, S. A. & Papa, F. R. The role of endoplasmic reticulum stress in human pathology. *Annu. Rev. Pathol.* **10**, 173–194 (2015).
6. Han, D. et al. IRE1α kinase activation modes control alternate endoribonuclease outputs to determine divergent cell fates. *Cell* **138**, 562–575 (2009).
7. Yoshida, H., Matsui, T., Yamamoto, A., Okada, T. & Mori, K. XBP1 mRNA is induced by ATF6 and spliced by IRE1 in response to ER stress to produce a highly active transcription factor. *Cell* **107**, 881–891 (2001).
8. Calfon, M. et al. IRE1 couples endoplasmic reticulum load to secretory capacity by processing the *XBP-1* mRNA. *Nature* **415**, 92–96 (2002).
9. Tirasophon, W., Welihinda, A. A. & Kaufman, R. J. A stress response pathway from the endoplasmic reticulum to the nucleus requires a novel bifunctional protein kinase/endoribonuclease (Ire1p) in mammalian cells. *Genes Dev.* **12**, 1812–1824 (1998).
10. Ghosh, R. et al. Allosteric inhibition of the IRE1α RNase preserves cell viability and function during endoplasmic reticulum stress. *Cell* **158**, 534–548 (2014).
11. Hollien, J. & Weissman, J. S. Decay of endoplasmic reticulum-localized mRNAs during the unfolded protein response. *Science* **313**, 104–107 (2006).
12. Hollien, J. et al. Regulated Ire1-dependent decay of messenger RNAs in mammalian cells. *J. Cell Biol.* **186**, 323–331 (2009).
13. Wang, L. et al. Divergent allosteric control of the IRE1α endoribonuclease using kinase inhibitors. *Nat. Chem. Biol.* **8**, 982–989 (2012).
14. Feldman, H. C. et al. Structural and functional analysis of the allosteric inhibition of IRE1α with ATP-competitive ligands. *ACS Chem. Biol.* **11**, 2195–2205 (2016).
15. Mendez, A. S. et al. Endoplasmic reticulum stress-independent activation of unfolded protein response kinases by a small molecule ATP-mimic. *eLife* **4**, e05434 (2015).
16. Ferri, E. et al. Activation of the IRE1 RNase through remodeling of the kinase front pocket by ATP-competitive ligands. *Nat. Commun.* **11**, 6387 (2020).
17. Lee, K. P. et al. Structure of the dual enzyme Ire1 reveals the basis for catalysis and regulation in nonconventional RNA splicing. *Cell* **132**, 89–100 (2008).
18. Korennykh, A. V. et al. Cofactor-mediated conformational control in the bifunctional kinase/RNase Ire1. *BMC Biol.* **9**, 48 (2011).
19. Prischi, F., Nowak, P. R., Carrara, M. & Ali, M. M. Phosphoregulation of Ire1 RNase splicing activity. *Nat. Commun.* **5**, 3554 (2014).
20. Maly, D. J. & Papa, F. R. Druggable sensors of the unfolded protein response. *Nat. Chem. Biol.* **10**, 892–901 (2014).
21. Harrington, P. E. et al. Unfolded protein response in cancer: IRE1α inhibition by selective kinase ligands does not impair tumor cell viability. *ACS Med. Chem. Lett.* **6**, 68–72 (2015).
22. Sanches, M. et al. Structure and mechanism of action of the hydroxy–aryl–aldehyde class of IRE1 endoribonuclease inhibitors. *Nat. Commun.* **5**, 4202 (2014).
23. Bantscheff, M. et al. Quantitative chemical proteomics reveals mechanisms of action of clinical ABL kinase inhibitors. *Nat. Biotechnol.* **25**, 1035–1044 (2007).
24. Golkowski, M. et al. Kinobead and single-shot LC–MS profiling identifies selective PKD inhibitors. *J. Proteome Res.* **16**, 1216–1227 (2017).
25. Golkowski, M. et al. Kinome chemoproteomics characterization of pyrrolo[3,4-*c*]pyrazoles as potent and selective inhibitors of glycogen synthase kinase 3. *Mol. Omics* **14**, 26–36 (2018).
26. Jan, C. H., Williams, C. C. & Weissman, J. S. Principles of ER cotranslational translocation revealed by proximity-specific ribosome profiling. *Science* **346**, 1257521 (2014).
27. Plumb, R., Zhang, Z. R., Appathurai, S. & Mariappan, M. A functional link between the co-translational protein translocation pathway and the UPR. *eLife* **4**, e07426 (2015).
28. Lerner, A. G. et al. IRE1α induces thioredoxin-interacting protein to activate the NLRP3 inflammasome and promote programmed cell death under irremediable ER stress. *Cell Metab.* **16**, 250–264 (2012).
29. Reimold, A. M. et al. Plasma cell differentiation requires the transcription factor XBP-1. *Nature* **412**, 300–307 (2001).
30. Iwakoshi, N. N. et al. Plasma cell differentiation and the unfolded protein response intersect at the transcription factor XBP-1. *Nat. Immunol.* **4**, 321–329 (2003).
31. Shaffer, A. L. et al. XBP1, downstream of Blimp-1, expands the secretory apparatus and other organelles, and increases protein synthesis in plasma cell differentiation. *Immunity* **21**, 81–93 (2004).
32. Tirosh, B., Iwakoshi, N. N., Glimcher, L. H. & Ploegh, H. L. XBP-1 specifically promotes IgM synthesis and secretion, but is dispensable for degradation of glycoproteins in primary B cells. *J. Exp. Med.* **202**, 505–516 (2005).
33. Kawahara, T., Yanagi, H., Yura, T. & Mori, K. Endoplasmic reticulum stress-induced mRNA splicing permits synthesis of transcription factor Hac1p/Ern4p that activates the unfolded protein response. *Mol. Biol. Cell* **8**, 1845–1862 (1997).
34. Cox, J. S. & Walter, P. A novel mechanism for regulating activity of a transcription factor that controls the unfolded protein response. *Cell* **87**, 391–404 (1996).
35. Kimmig, P. et al. The unfolded protein response in fission yeast modulates stability of select mRNAs to maintain protein homeostasis. *eLife* **1**, e00048 (2012).
36. Papa, F. R., Zhang, C., Shokat, K. & Walter, P. Bypassing a kinase activity with an ATP-competitive drug. *Science* **302**, 1533–1537 (2003).
37. Tong, M. & Seeliger, M. A. Targeting conformational plasticity of protein kinases. *ACS Chem. Biol.* **10**, 190–200 (2015).
38. Jura, N. et al. Catalytic control in the EGF receptor and its connection to general kinase regulatory mechanisms. *Mol. Cell* **42**, 9–22 (2011).
39. Zhang, K. et al. The unfolded protein response sensor IRE1α is required at 2 distinct steps in B cell lymphopoiesis. *J. Clin. Invest.* **115**, 268–281 (2005).
40. Iwawaki, T., Akai, R., Yamanaka, S. & Kohno, K. Function of IRE1α in the placenta is essential for placental development and embryonic viability. *Proc. Natl Acad. Sci. USA* **106**, 16657–16662 (2009).
41. S. Morita, S. A. et al. Targeting ABL–IRE1α signaling spares ER-stressed pancreatic β-cells to reverse autoimmune diabetes. *Cell Metab.* **25**, 883–897 (2017).
42. Sato, H., Shiba, Y., Tsuchiya, Y., Saito, M. & Kohno, K. 4μ8C inhibits insulin secretion independent of IRE1α RNase activity. *Cell Struct. Funct.* **42**, 61–70 (2017).
43. Papandreou, I. et al. Identification of an Ire1α endonuclease specific inhibitor with cytotoxic activity against human multiple myeloma. *Blood* **117**, 1311–1314 (2011).
44. Grandjean, J. et al. Pharmacologic IRE1/XBP1s activation confers targeted ER proteostasis reprogramming. *Nat. Chem. Biol.* **16**, 1052–1061 (2020).

Methods

Expression and purification of IRE1α* and dpIRE1α*. A construct containing the cytosolic kinase and RNase domains of human IRE1α (residues 547–977; IRE1α*) was expressed in SF9 insect cells (ATCC, CRL-1711) by using the Bac-to-Bac baculovirus expression system (Invitrogen) with a His_6 tag at the N terminus and was purified with a nickel–nitriloacetic acid (Qiagen) column. To generate dpIRE1α*, we removed basal phosphorylation sites by incubating IRE1α* with lambda protein phosphatase (λ-PPase; New England Biolabs) at a molar ratio of 5:1 (IRE1α*:λ-PPase) in 50 mM HEPES pH 7.5, 100 mM NaCl, 1 mM $MnCl_2$, 2 mM dithiothreitol (DTT) and 0.01% Brij 35 detergent (vol/vol) overnight at 4 °C. Dephosphorylation was verified through western blotting using a universal phosphoprotein detection agent (biotin-pIMAGO; Tymora Analytical Operations, FL800) and imaged using a streptavidin-linked fluorophore.

Western blotting and antibodies. For protein analysis, cells were lysed into modified RIPA buffer (50 mM Tris, 150 mM NaCl, 10 mM NaF, 1% NP-40 (vol/vol), 0.25% sodium deoxycholate (wt/vol), 5% glycerol (vol/vol), pH 7.8) containing protease inhibitor (Pierce Protease Inhibitor Tablets and 1 mM phenylmethylsulfonyl fluoride (PMSF)) and phosphatase inhibitor (Phosphatase Inhibitor Cocktails 2 and 3, Sigma Aldrich) before gel loading. Western blots were performed using Any kD Mini-PROTEAN TGX Precast protein gels (Bio-Rad). Gels were run using Tris-glycine running buffer (25 mM Tris pH 8.6, 192 mM glycine, 0.1% SDS (wt/vol)) at 180 V. Gels were transferred to nitrocellulose paper using the TransBlot Turbo System (Bio-Rad) at 25 V and 2.5 A for 15 min. Nitrocellulose blots were blocked for 30 min at room temperature with Odyssey blocking buffer (Li-Cor). Primary antibodies were diluted into blocking buffer and incubated overnight at 4 °C. Blots were washed twice with TBST (20 mM Tris pH 7.5, 150 mM NaCl, 0.1% Tween-20) and incubated with near-infrared dye-conjugated secondary antibodies (Li-Cor) for 1 h at room temperature (dilution 1:10,000). Blots were imaged using a Li-Cor Odyssey IR imager and quantitated using ImageStudio. The following primary antibodies were used in this study: rabbit anti-IRE1α mAb 14C10 (Cell Signaling, 3294; dilution 1:1,000), rabbit anti-spliced XBP1 (Cell Signaling, 12782; dilution 1:1,000), rabbit anti-caspase-3 (Cell Signaling, 9662; dilution 1:1,000), mouse anti-proinsulin (Santa Cruz Biotechnology, sc-9168; dilution 1:1,000) and rabbit anti-GAPDH (Santa Cruz Biotechnology, sc-25778; dilution 1:1,000).

In vitro kinase inhibition assays. Inhibitors (initial concentration of 10 or 60 μM, threefold serial dilutions) were incubated with IRE1α* in cleavage buffer (20 mM HEPES, 0.05% Triton X-100 (vol/vol), 50 mM KCl, 1 mM $MgCl_2$, 1 mM DTT, pH 7.5) for 30 min, followed by incubation with 10 μCi [γ^{32}P]ATP (3,000 Ci mmol^{-1}; PerkinElmer) at 23 °C for 3 h. Samples were then spotted onto glass fiber paper (Easytab-C Glass Fiber Filter Paper, PerkinElmer), washed twice with 0.5% phosphoric acid and autoradiographed using a GE Typhoon FLA 9000 Imager. Blots were quantitated using ImageQuant software. The percent inhibition was quantified by setting the background (no kinase well) as 0 and standardizing to IRE1α* without compound treatment (IRE1α* + DMSO). Dose–response curves were fit using the 'one-site fit logIC50' parameter using GraphPad Prism V.8 analysis software.

In vitro RNase inhibition assays. IRE1α* (50 nM) was incubated with inhibitor (initial concentration of 10 or 60 μM, threefold serial dilutions) or DMSO for 30 min in assay buffer (20 mM Tris, 50 mM NaCl, 1 mM $MgCl_2$, 2 mM DTT, 0.05% Triton X-100 (vol/vol), pH 7.5). Assays were initiated by adding 10 μl of XBP1 minisubstrate (5′-Alex647-CAUGUCCGCAGCGCAUG-IowaBlack-RQ-3′; IDT) to the wells at a final concentration of 200 nM and a final well volume of 30 μl. Fluorescence was detected on a PerkinElmer Envision Microplate Reader at excitation and emission wavelengths of 650 nm and 665 nm, respectively. Dose–response curves were fit using the 'one-site fit logIC50' parameter using GraphPad Prism V.8 analysis software. Residual RNase activity (Fig. 2f and Extended Data Fig. 4) was determined by subtracting maximally achieved percent RNase inhibition (indicated by the plateau of the dose–response curve) from maximally achieved percent kinase inhibition (indicated by the plateau of the dose–response curve).

In vitro determination of IRE1α*–inhibitor complex K_{dimer} values. IRE1α* or dpIRE1α* was titrated from either 2 μM or 4 μM in twofold serial dilutions in assay buffer (20 mM Tris, 50 mM NaCl, 1 mM $MgCl_2$, 2 mM DTT, 0.05% Triton X-100 (vol/vol), pH 7.5) and incubated with 50 μM inhibitor for 30 min at room temperature. Assays were initiated by adding 10 μl of XBP1 minisubstrate (5′-Alex647-CAUGUCCGCAGCGCAUG-IowaBlack-RQ-3′; IDT) to the wells at a final concentration of 6 μM and a final well volume of 30 μl. Fluorescence was detected on a PerkinElmer Envision Microplate Reader at excitation and emission wavelengths of 650 nm and 665 nm, respectively. The reaction process was monitored in real time in 10-s intervals for at least 30 min. Initial rates of XBP1 cleavage were determined for each respective IRE1α* of dpIRE-1α* concentration. Specific activity was then determined by dividing rate (relative fluorescence units (RFU) per s) by the respective IRE1α* or dpIRE1α* concentration used (RFU per s/concentration of IRE1α). K_{dimer} values were determined by fitting these values using the non-linear regression 'one-site total' binding parameter in GraphPad Prism V.8 analysis software.

Crystallization of IRE1α* and PAIR1. *Protein production and crystallization.* Expression of IRE1α was performed by Proteros according to previously established protocols. A purification protocol was established, and homogeneous protein was produced in preparative amounts using affinity and gel filtration chromatography steps. This procedure yielded homogenous protein with a purity greater than 95% as judged from Coomassie stained SDS–PAGE. This purified protein was used in crystallization trials using both a standard screen with approximately 1,200 different conditions and as crystallization conditions identified using literature data. Conditions initially obtained have been optimized using standard strategies, systematically varying parameters critically influencing crystallization, such as temperature, protein concentration, drop ratio and others. These conditions were also refined by systematically varying pH or precipitant concentrations.

Data collection and processing. A cryoprotocol was established using PROTEROS Standard Protocols. Crystals were flash frozen and measured at a temperature of 100 K. The X-ray diffraction data were collected from complex crystals of IRE1α with the ligand PAIR1 at the SWISS LIGHT SOURCE using cryogenic conditions. The X-ray source was PXII/X10SA, and the wavelength was 1.0000 Å. The crystals belong to space group *C*2. Data were processed using the programs XDS and XSCALE.

Structural modeling and refinement. The phase information necessary to determine and analyze the structure was obtained by molecular replacement. A previously solved structure of IRE1α was used as a search model. Subsequent model building and refinement were performed according to standard protocols with the software packages CCP4 and COOT. For the calculation of the free *R*-factor, a measure to cross-validate the correctness of the final model, about 2.6% of measured reflections were excluded from the refinement procedure (Supplementary Table 1). TLS refinement (using REFMAC5, CCP4) was performed, which resulted in lower *R*-factors and higher quality of the electron density map. Automatically generated local non-crystallographic symmetry restraints were applied (keyword 'ncsr local' of newer REFMAC5 versions). The ligand parameterization and generation of the corresponding library files were performed with CORINA. The water model was built with the 'Find waters' algorithm of COOT by putting water molecules in peaks of the F_o–F_c map contoured at 3.0 followed by refinement with REFMAC5 and checking all waters with the validation tool of COOT. The criteria for the list of suspicious waters were *B*-factor greater than 80 Å^2, $2F_o$–F_c map less than 1.2σ and distance to closest contact less than 2.3 Å or more than 3.5 Å. The suspicious water molecules and those in the ligand-binding site (distance to ligand less than 10 Å) were checked manually. The Ramachandran plot of the final model shows 92.6% of all residues in the most favored region, 6.7% in the additionally allowed region and 0.4 % in the generously allowed region. The residues Met 872(A) and Met 872(B) are found in the disallowed region of the Ramachandran plot. They were either confirmed by the electron density map or could not be modeled in another sensible conformation. Structural analysis was performed using Pymol version 2.0.5.

Kinome profiling and selectivity. *Kinobead enrichment protocol.* HEK293 and HCT116 cells were plated on 15-cm plates until 90% confluent and were lysed into 750 μl of modified RIPA buffer (50 mM Tris, 150 mM NaCl, 10 mM NaF, 1% NP-40, 0.25% sodium deoxycholate, 5% glycerol, pH 7.8) containing protease inhibitor (Pierce Protease Inhibitor Tablets and 1 mM PMSF) and phosphatase inhibitor (Phosphatase Inhibitor Cocktails 2 and 3, Sigma Aldrich). Protein content was determined via Bradford assay. HEK293 and HCT116 lysates were combined in a 1:1 ratio, and exogenous IRE1α* was added to the lysate at a final concentration of 33.3 nM. Lysate (300 μg per sample) was incubated and rotated end over end with 10 μM inhibitor or DMSO (1% vol/vol) for 1 h at 4 °C. For kinase enrichment, 10 μl of 50% kinobead slurry (in 20% ethanol) was prepared by washing twice with 500 μl of modified RIPA buffer. DMSO- or inhibitor-treated lysates were then added to the washed kinobeads and rotated end over end for 3 h at 4 °C. After enrichment, the supernatant was aspirated off and the beads were washed twice with 500 μl of ice-cold modified RIPA buffer and three times with 500 μl of ice-cold TBS (50 mM Tris, 150 mM NaCl, pH 7.8) to remove detergent. Beads were resuspended in 25 μl of denaturing buffer (6 M guanidinium chloride, 50 mM Tris containing 5 mM TCEP and 10 mM CAM, pH 8.5). The bead slurries in denaturing buffer were then heated to 95 °C for 5 min. After, the bead slurries were diluted twofold with 100 mM TEAB (pH 8.5). Then, 0.4 μg of LysC (Wako) was added to the beads, and the pH was adjusted to 8 to 9 with 1 N NaOH. The mixture was agitated on a Thermomixer (Eppendorf) at 37 °C for 2 h at 1,400 rpm. After, the samples were diluted twofold with 100 mM TEAB, and 0.4 μg of sequencing-grade trypsin (Pierce) was added and the samples were agitated for another 12 h at 37 °C at 800 rpm in the Thermomixer. After the overnight trypsinization, samples were diluted twofold with Buffer A (5% acetonitrile, 0.1% trifluoroacetic acid) containing 1% formic acid, and the pH was adjusted to 2 to 3 with formic acid if necessary. Homemade StageTips were prepared by running 50 μl of Buffer B (80% acetonitrile, 0.1% trifluoroacetic acid, water) through them followed by 50 μl of

Buffer A (5% acetonitrile, 0.1% trifluoroacetic acid, water)[45]. Beads were spun down and supernatant was added directly to StageTips. Following sample loading, StageTips were washed with 50 µl of Buffer A and eluted with 50 µl of Buffer B. Samples were speed vacuumed until dry and resuspended in Buffer A for injection onto liquid chromatography–mass spectrometry (LC–MS)[24].

LC–MS and data analysis. Tryptic peptides were separated using a nanoAcquity UPLC instrument with 10-cm fused silica capillary columns made in house and packed with 5-µm, 120-Å reverse-phase C18 beads (ReproSil-Pur, Maisch). Liquid chromatography was performed over 120 min using an initial 20-min isocratic trapping of 3% Buffer B and a flow rate of 700 nl min^{-1} followed by a 100-min gradient of 35% Buffer B to 80% Buffer B at 350 nl min^{-1}. LC Buffer A solvent was 0.1% acetic acid in water, and LC Buffer B was 99.9% acetonitrile and 0.1% acetic acid. MS data were analyzed using a Thermo Orbitrap Fusion Tribrid. Raw files were analyzed using MaxQuant (Andromeda) version 1.6.0.16. Files were analyzed further using Perseus (version 1.6.0.7) by filtering LFQ intensity values only identified by site, reverse or potential contaminant. Missing LFQ intensity values were imputed in Perseus from a standard distribution downshifted by 1.8 and having a width of 0.4. To determine kinases that were significantly competed by treatment with 10 µM inhibitor, we applied a two-tailed two-sample *t*-test in Perseus with an FDR of 0.05. Kinases were reported as being non-competed by an inhibitor if it had a $\log_2$ LFQ ratio ($\log_2$ difference) of <1.0. Kinome tree visualization plots were created using CORAL, and heat maps were made using GraphPad Prism V.8 (ref. [46]). A detailed explanation of MS settings and search parameters, in addition to the complete proteomic dataset, can be found in Supplementary Dataset 1.

Phostag acrylamide gels. *Treatment conditions for phostag gels.* INS-1 cells or IRE1α-overexpressing isogenic INS-1 cells were plated onto a 24-well poly-D-lysine-coated tissue culture plate and grown for 48 h. Inhibitor or DMSO were added to the medium and incubated for 1 h at 37 °C with 5% CO_2 before addition of ER stress agents. After the 1-h inhibitor incubation, cells were treated with 200 µg ml^{-1} brefeldin A (BFA; Sigma, B6542) for 2 h or 5 ng ml^{-1} Dox (Sigma) for 6 h, with care to ensure the total DMSO concentration in the medium did not exceed 1% (vol/vol). Cells were lysed directly into SDS loading buffer (50 mM Tris, 100 mM DTT, 2% SDS (wt/vol), 10% glycerol (vol/vol) and 0.1% bromophenol blue (wt/vol), pH 6.8) and boiled for 5 min before gel loading.

Phostag acrylamide gel procedure. The IRE1α phostag acrylamide gel recipe has been previously established and was followed verbatim for this study[47]. Resolving gels were allowed to solidify (~1.5 h) before adding the stacking gel and comb, which was then allowed to solidify (~1 h). Gels were run using Tris-glycine-SDS running buffer (25 mM Tris, 192 mM glycine, 0.1% SDS, pH 8.3) at 100 V for 3–3.5 h. After the gels were run, they were transferred onto nitrocellulose membranes via rapid transfer using a Transblot Turbo and premade transfer packs. Gels were transferred at 25 V and 2.5 A for 15 min. Nitrocellulose membranes were then subjected to standard western blotting procedures.

Tissue culture. INS-1 cells (rat insulinoma β-cells) were grown in RPMI medium supplemented with 10% fetal bovine serum (FBS) (vol/vol), 1 mM sodium pyruvate, 10 mM HEPES, 2 mM glutamine and 50 µM β-mercaptoethanol on poly-D-lysine-coated tissue culture flasks. IRE1α (murine) was cloned into pcDNA5/FRT/TO. INS-1 FRT/TO cells were grown following the protocol above. INS-1 FRT/TO cells were transfected with 2 µg of IRE1α-pcDNA5/FRT/TO and 2 µg of pOG44 using Lipofectamine 2000 (Thermo Fisher). Cell medium was exchanged the next day, and cells were grown for another day before passaging. Selection was performed using 50 µg ml^{-1} hygromycin B (Thermo Fisher) over about 2 weeks until all untransfected cells died and colonies appeared in transfected cells. Stably integrated cells were maintained in RPMI medium supplemented with 10% FBS (vol/vol), 1 mM sodium pyruvate, 10 mM HEPES, 2 mM glutamine, 50 µM β-mercaptoethanol and 25 µg ml^{-2} hygromycin B. HEK293 cells (ATCC, CRL-1573) were grown in DMEM high-glucose medium (Gibco) supplemented with 10% FBS. HCT116 (ATCC, CCL-247) cells were maintained in McCoy's 5A modified medium (Gibco) supplemented with 10% FBS. Non-diabetic human islets were obtained from Prodo Labs and cultured in supplemented Prodo Islet Medium (PIM(S) from Prodo Labs). All cells lines were maintained at 37 °C with 5% CO_2.

RNA isolation, qPCR and primers. INS1 or isogenic IRE1α-overexpressing INS-1 cells were plated onto poly-D-lysine-coated tissue culture plates and grown for 48 h. Inhibitors or DMSO were added to the medium and incubated for 1 h at 37 °C with 5% CO_2 before addition of ER stress agents or Dox as indicated. Islets were pretreated with either DMSO, PAIR1 or KIRA9 for 2 h at 37 °C with 5% CO_2 followed by treatment with 2.5 mM DTT for 2 h. RNA was isolated from whole cells using either QIAGEN RNeasy Mini kits or Trizol (Invitrogen) and 1 µg total RNA was reverse transcribed using the QuantiTect Reverse Transcription Kit (Qiagen) to obtain total cDNA. Then, XBP1 primers were used to amplify an XBP1 amplicon spanning the 26-nt intron from the cDNA samples in a regular three-step PCR. Thermal cycles were 5 min at 95 °C, 30 cycles of 30 s at 95 °C, 30 s at 60 °C and 1 min at 72 °C, followed by 72 °C for 15 min and hold at 4 °C. Primers used for *Xbp1* mRNA splicing were as follows: for rat (sense primer XBP1.3S (5′-AAACAGAGTAGCACAGACTGC-3′) and antisense primer XBP1.2AS (5′-GGATCTCTAAGACTAGAGGCTTGGTG-3′)) and for human (sense primer XBP1.1S (5′-AAACAGAGTAGCAGCTCAGACTGC-3′) and antisense XBP1.2AS (5′-TCCTTCTGGGTAGACCTCTGG-3′)). PCR fragments were then digested by PstI, resolved on 3% agarose gels, stained with ethidium bromide and quantified by densitometry using ImageJ (NIH). For standard mRNA detection by qPCR, we used SYBR green (QIAGEN) and a StepOnePlus Real-Time PCR System (Applied Biosystems). Thermal cycles were 5 min at 95 °C and 40 cycles of 15 s at 95 °C and 30 s at 60 °C. Gene expression levels were normalized to *Actb*. Primers used for qPCR of RIDD targets were as follows: *Actb*, forward 5′-GCAAATGCTTCTAGGCGGAC-3′ and reverse 5′-AAGAAA GGGTGTAAAACGCAGC-3′; *Ins1*, forward 5′-GTCCTCTGGGAGCCCAAG-3′ and reverse 5′-ACAGAGCCTCCACCAGG-3′; *Ins2*, forward 5′-ATCCTCTGG GAGCCCCGC-3′ and reverse 5′-AGAGAGCTTCCACCAAG-3′; *Bloc1s1*, forward 5′-CAAGGAGCTGCAGGAGAAGA-3′ and reverse 5′-GCCTGG TTGAAGTTCTCCAC-3′.

Annexin V staining. For assaying apoptosis by annexin V staining, cells were plated in 12-well plates overnight. Cells were then treated with various reagents for indicated time periods. On the day of flow cytometry analysis, cells were trypsinized and washed in PBS and resuspended in Annexin V-binding buffer with Annexin V fluorescein isothiocyanate (BD Pharmingen). Flow cytometry was performed on a BD Biosciences LSR II flow cytometer.

RNA-seq. *RNA isolation and preparation.* Isogenic IRE1α-overexpressing INS-1 cells were pretreated with inhibitors for 1 h followed by addition of 5 ng ml^{-1} Dox for 4 h or 24 h. All conditions for RNA-seq analysis were performed in three biological replicates. RNA was isolated from whole cells using a Qiagen RNeasy with genomic DNA eliminator kit. RNA purity was determined using a NanaPhotometer spectrometer (IMPLEN). RNA integrity and quantitation were assessed using the RNA Nano 6000 Assay kit and Bioanalyzer 2100 system (Agilent Technologies).

Library preparation, clustering and sequencing. Library preparation for RNA-seq was performed by Novogene. A total amount of 1 µg of RNA per sample was used as input material for the RNA sample preparations. Sequencing libraries were generated using an NEBNext Ultra RNA Library Prep kit for Illumina (NEB) following manufacturer's recommendations, and index codes were added to attribute sequences to each sample. Briefly, mRNA was purified from total RNA using poly-T oligo-attached magnetic beads. Fragmentation was carried out using divalent cations under elevated temperature in NEBNext First Strand Synthesis Reaction Buffer (5×). First-strand cDNA was synthesized using random hexamer primer and MMuLV reverse transcriptase (RNase H). Second-strand cDNA synthesis was subsequently performed using DNA polymerase I and RNase H. Remaining overhangs were converted into blunt ends via exonuclease/polymerase activities. After adenylation of 3′ ends of DNA fragments, NEBNext Adaptors with hairpin loop structure were ligated to prepare for hybridization. To select cDNA fragments of preferentially 150–200 bp in length, the library fragments were purified with an AMPure XP system (Beckman Coulter). Then, 3 µl of USER Enzyme (NEB) was used with size-selected, adaptor-ligated cDNA at 37 °C for 15 min followed by 5 min at 95 °C before PCR. PCR was performed with Phusion High-Fidelity DNA polymerase, Universal PCR primers and Index (X) Primer. Finally, PCR products were purified (AMPure XP system), and library quality was assessed on the Agilent Bioanalyzer 2100 system. The clustering of the index-coded samples was performed on a cBot Cluster Generation System using PE Cluster Kit cBot-HS (Illumina) according to the manufacturer's instructions. After cluster generation, the library preparations were sequenced on an Illumina platform, and 125-bp × 150-bp paired-end reads were generated.

Quality control and genome mapping. Raw data (raw reads) of fastq format were first processed using Novogene Perl scripts. In this step, clean data (clean reads) were obtained by removing reads containing adapter, reads containing ploy-N and low-quality reads from raw data. Q20 and Q30 scores and GC content of the clean data were calculated. All the downstream analyses were based on the clean data with high quality. Reference genome and gene model annotation files were downloaded from the genome website directly. The index of the reference genome was built using HISAT2 2.1.0, and paired-end clean reads were aligned to the reference genome using HISAT2 version 2.1.0beta allowing 2 mismatches; and assigned to genes using HTSeq 0.6.1 (-m union).

Gene expression analysis. Differential gene expression analysis and log-fold-change estimates were obtained using DESeq2. Heatmaps were plotted using regularized-log (rlog) transformed data, normalized to the rlog-mean expression of the untreated samples. For RIDD gene analysis, the INS-1 RIDD signature and annotation of type was previously described[6]. For whole-secretome analysis, high-confidence human genes encoding secreted proteins were defined as

previously described[26], and the rat orthologs defined according to the Mouse Genome Institute (MGI) mammalian orthology database. Statistical significance testing in the cumulative distributions of log-transformed fold-changes was performed using the two-sided Wilcoxon rank-sum test. For inhibition of apoptosis gene analysis, *R. norvegicus* genes in Gene Ontology term GO0043065 (positive regulation of apoptotic process) were filtered for genes upregulated by 1.5-fold with adjusted P values < 0.01 after doxycycline treatment and heatmaps were generated as described above. For comparison of the *Ern1* transgene and endogenous expression, reads were mapped using Bowtie2 to a custom genome consisting of the rat *Ern1* coding sequence and the mouse *Ern1* coding sequence. Reads uniquely mapping to one or the other coding sequence were assigned to the endogenous locus or to the transgene, respectively. To calculate *Xbp1* splicing, the read coverage over each base in the rat *Xbp1* exon 4 was calculated using the Bedtools genomecov function (-d -split). To quantify unspliced *Xbp1*, the coverage was averaged over all the nucleotides in the non-canonical intron. To quantify the total *Xbp1* expression, the coverage was averaged over all the nucleotides in exon 4, excluding those nucleotides in the non-noncanonical intron. Spliced *Xbp1* (read coverage ratio) was calculated as [1 − (unspliced *Xbp1*/total *Xbp1*)].

Splenocyte isolation and plasma cell differentiation. Splenocytes were isolated from C57BL/6 mice into single-cell suspensions in complete medium containing RPMI 1640, L-glutamine (Corning-Gibco), penicillin/streptomycin L-glutamine (Life Technologies), 10 mM HEPES buffer (Life Technologies), non-essential amino acids (Life Technologies), 1 mM sodium pyruvate (Life Technologies), 55 mM β-mercaptoethanol (Gibco) and 10% heat-inactivated FBS (Omega Scientific). Red blood cells were lysed with ammonium chloride potassium buffer. Cells were loaded with CellTrace Violet (CTV; Invitrogen) per the manufacturer's instructions except at 5×10^6 cells per ml rather than at 1×10^6 cells per ml. Splenocytes were plated at 2.5×10^5 cells per well in a 96-well round-bottom plate in complete medium. The splenocytes were treated with or without 1 μg ml^{-1} LPS 026:b6 (Sigma). Twofold serial dilutions of IRE-1α inhibitors (20 μM–1.25 μM) were prepared in DMSO and added to the LPS-treated cells at a final dilution of 1:2,000. The splenocytes were incubated for 3 d in a humidified chamber maintained at 37 °C and 5% CO_2 before collection and staining for flow cytometry.

Flow cytometry. Cells from the plasma cell assay were collected in a 96-well plate and washed with PBS followed by staining with a LIVE/DEAD Fixable Near-IR Dead Cell Stain kit (Invitrogen). Reagent was reconstituted per the manufacturer's instructions and diluted 1:1,000 in PBS, and cells were stained in 100 μl on ice for 20 min. The cells were then washed with FACS buffer, PBS (Corning), 2 mM EDTA and 2% heat-inactivated FBS (Omega Scientific). The cells were then stained with 50 μl of antibody cocktail consisting of anti-CD19 (BioLegend), anti-CD45R (BD Pharmingen) and anti-CD138 (BioLegend) in FACS buffer on ice for 15 min. Cells were washed twice with 200 μl of FACS buffer. XBP1 staining was performed using a Foxp3/transcription factor buffer set (eBioscience) per the manufacturer's instructions in conjunction with AlexaFluor 647 anti-XBP1s (BD Biosciences). Cells were resuspended in FACS buffer and combined with an equal volume of 4% paraformaldehyde with 5000 Countbright Absolute Counting Beads (Thermo Fisher). Stained cells were analyzed on a Fortessa (Becton Dickinson). Division index and data analyses were performed using FlowJo (v10) software (Treestar).

ELISA for secreted IgM. Media supernatants from the in vitro plasma cell differentiation assay were measured for secreted IgM by ELISA. Plates (96-well; Costar, 3690) were coated with 1 μg ml^{-1} goat anti-IgM (Southern Biotech, 1020–01) in PBS. Wash buffer (PBS with 0.05% Tween-20 (vol/vol)) was used for all washing steps, and samples were blocked with PBS-BB (PBS without Ca^{2+}/Mg^{2+}, 1% bovine serum albumin (BSA; wt/vol), 0.05% Tween-20 (vol/vol)). Supernatants from LPS-stimulated samples were diluted (1:100) and medium-only samples were diluted (1:10) in PBS-BB. IgM standard (Southern Biotech, 0101-01) was prepared in a twofold serial dilution in PBS-BB. IgM was detected with goat anti-IgM-horseradish peroxidase (HRP) (Southern Biotech, 1020-05) diluted (1:3,000) in PBS-BB. ELISA plates were developed with TMB (Sigma) and stopped with 1 N sulfuric acid. Absorbance was measured at 450 nm using a spectrophotometer (Spectramax M5, Molecular Devices). Sample IgM concentration values were calculated with SoftMaxPro v7 software.

Synthesis of IRE1α modulators. See Supplementary Information and Note.

Statistical analysis. Quantitative data are presented as mean ± s.e.m., as specified in the figure legends. Information regarding the number of replicates or samples and statistical analyses are described in the corresponding figure and table legends.

Material availability. Requests for materials should be addressed to F.R.P. or D.J.M.

Reporting Summary. Further information on research design is available in the Nature Research Reporting Summary linked to this article.

Data availability

Kinome selectivity data are provided in Supplementary Dataset 1. Coordinates and structure factors have been deposited in the PDB under accession code 7BMK. Cell line RNA-seq data have been deposited to the Gene Expression Omnibus (GEO)[48] and are accessible through GEO Series accession number GSE164496 (https://www.ncbi.nlm.nih.gov/geo/query/acc.cgi?acc=GSE164496). The KEGG database used in this study was acquired from http://www.genome.jp/kegg/. Source data are provided with this paper.

References

45. Yu, Y., Pieper, R. & Smith, M. A spinnable and automatable StageTip for high throughput peptide desalting and proteomics. *Protoc. Exch.* https://doi.org/10.1038/protex.2014.033 (2014).
46. Metz, K. S. et al. Coral: clear and customizable visualization of human kinome data. *Cell Syst.* **7**, 347–350 (2018).
47. Qi, L., Yang, L. & Chen, H. Detecting and quantitating physiological endoplasmic reticulum stress. *Methods Enzymol.* **490**, 137–146 (2011).
48. Edgar, R., Domrachev, M. & Lash, A. E. Gene Expression Omnibus: NCBI gene expression and hybridization array data repository. *Nucleic Acids Res.* **30**, 207–210 (2002).

Acknowledgements

This work was supported by the Leona M. and Harry B. Helmsley Charitable Trust (G-3231 to F.R.P.), the Juvenile Diabetes Research Foundation (JDRF 2-SRA-2016-234-S-N to F.R.P.) and the NIH (R01DK116064 to D.J.M. and F.R.P.; R01DK100623 to B.J.B, D.J.M. and F.R.P.; U01DK123609 to D.J.M. and F.R.P.; R01HL145037 to F.R.P.; K08HL157654 to V.C.A.; R01AR069520 to J.Z. and R01AI148487 to J.Z.).

Author contributions

H.C.F. executed all enzymatic and biochemical analyses. H.C.F. and B.J.B. designed compounds. H.C.F. and V.N.V. synthesized and characterized compounds. R.G., J-H.K. and A.O. performed cellular analysis of XBP1 splicing, RIDD and apoptosis. V.C.A. conducted RNA-seq analyses. H.C.F. and Z.E.P. performed target engagement studies. H.C.F. and B.G.K.P. performed chemoproteomic profiling. Plasma cell differentiation studies were designed by J.Z. and performed by J.L.M. J.Z., F.R.P. and D.J.M. supervised experiments. H.C.F., F.R.P. and D.J.M. wrote the manuscript with input from all authors. F.R.P. and D.J.M. conceived of and led this study.

Competing interests

B.J.B., F.R.P. and D.J.M. are founders, equity holders and consultants for OptiKIRA, LLC (Cleveland, OH), a biotech company founded on the treatment of ER-stress-induced retinal degeneration; no company funding or chemical matter supported the work in this manuscript. J.Z. serves on the SAB for Walking Fish Therapeutics.

Additional information

Extended data is available for this paper at https://doi.org/10.1038/s41589-021-00852-0.

Supplementary information The online version contains supplementary material available at https://doi.org/10.1038/s41589-021-00852-0.

Correspondence and requests for materials should be addressed to Feroz R. Papa or Dustin J. Maly.

Peer review information *Nature Chemical Biology* thanks Nathanael Gray, Boaz Tirosh and the other, anonymous, reviewer(s) for their contribution to the peer review of this work.

Reprints and permissions information is available at www.nature.com/reprints.

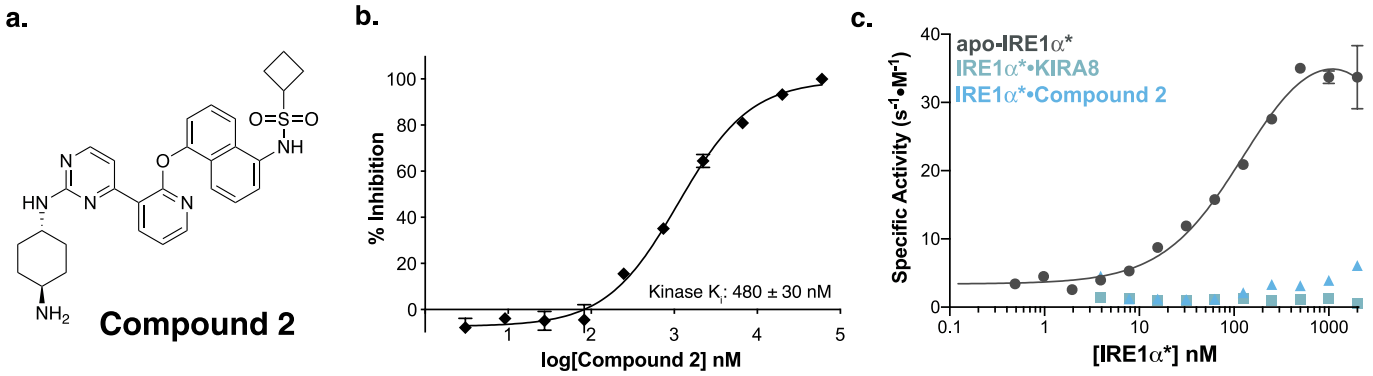

Extended Data Fig. 1 | KIRAs monomerize IRE1α*. (**a**) Chemical structure of compound **2**. (**b**) Inhibition of IRE1α*'s kinase activity by compound **2** (K_i = 480 nM). Data points shown are the mean of n = 3 independent experiments ± SEM. **(c)** K_{dimer} curve of the IRE1α*-compound **2** complex (*teal*). K_{dimer} curves of *apo* IRE1α* (dark gray) and the IRE1α*-KIRA8 complex (*light blue*) from Fig. 1e are shown for comparison. Data points shown are the mean of n = 3 independent experiments ± SEM.

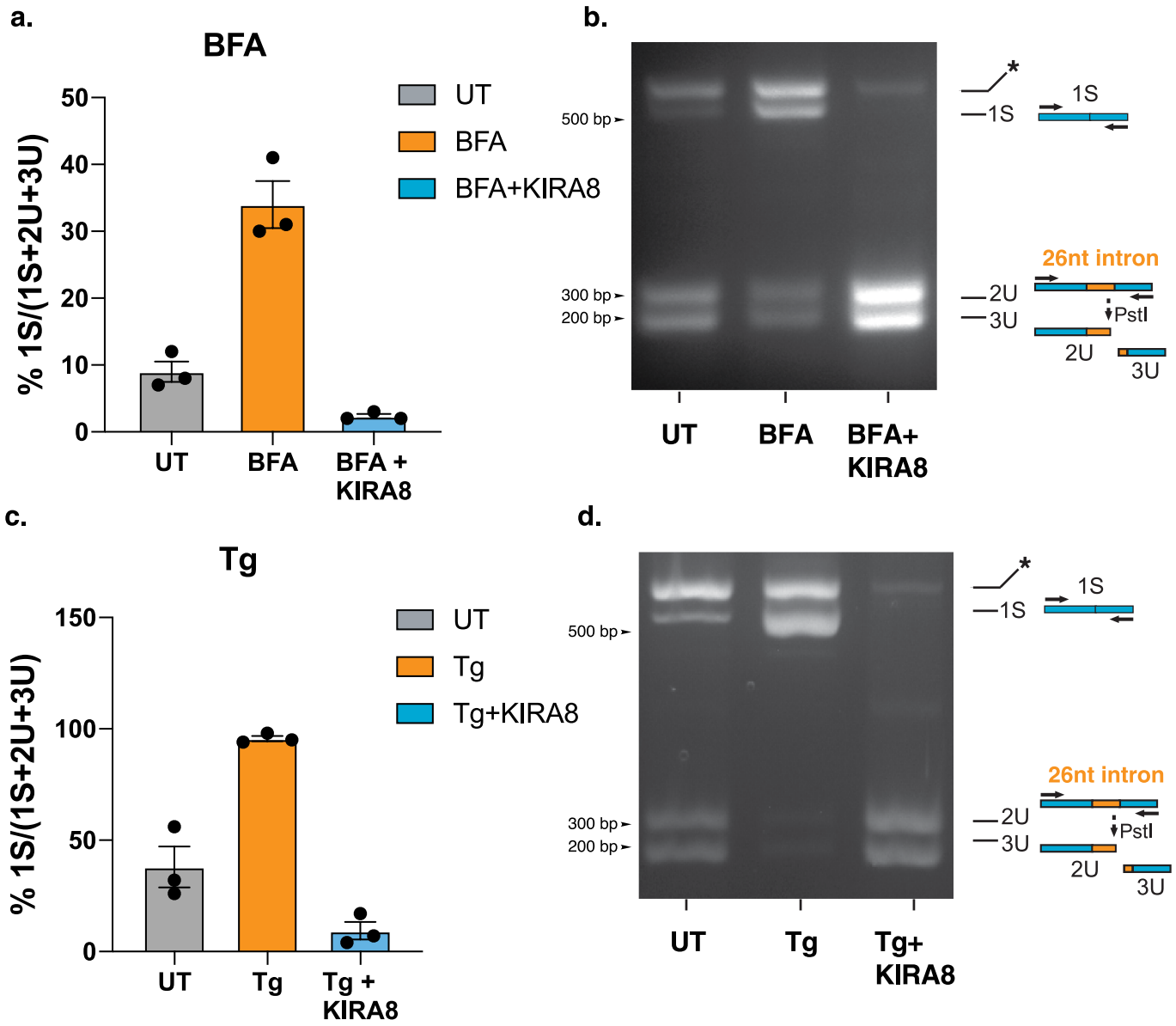

Extended Data Fig. 2 | KIRA8 completely suppresses XBP1 splicing in ER-stressed INS-1 cells. (**a**) Quantification of spliced XBP1 in untreated parent INS-1 cells and parent INS-1 cells treated with brefeldin A (BFA) or BFA and KIRA8. Values shown are the mean of n = 3 biologically independent samples ± SEM. (**b**) Representative example of an EtBr-stained agarose gel of XBP1 cDNA amplicons from INS-1 cells subjected to the conditions described in (**a**). (**c**) Quantification of spliced XBP1 in untreated parent INS-1 cells and parent INS-1 cells treated with thapsigargin (Tg) or Tg and KIRA8. Values shown are the mean of n = 3 biologically independent samples ± SEM. (**d**) Representative example of an EtBr-stained agarose gel of XBP1 cDNA amplicons from INS-1 cells subjected to the conditions described in (**c**).

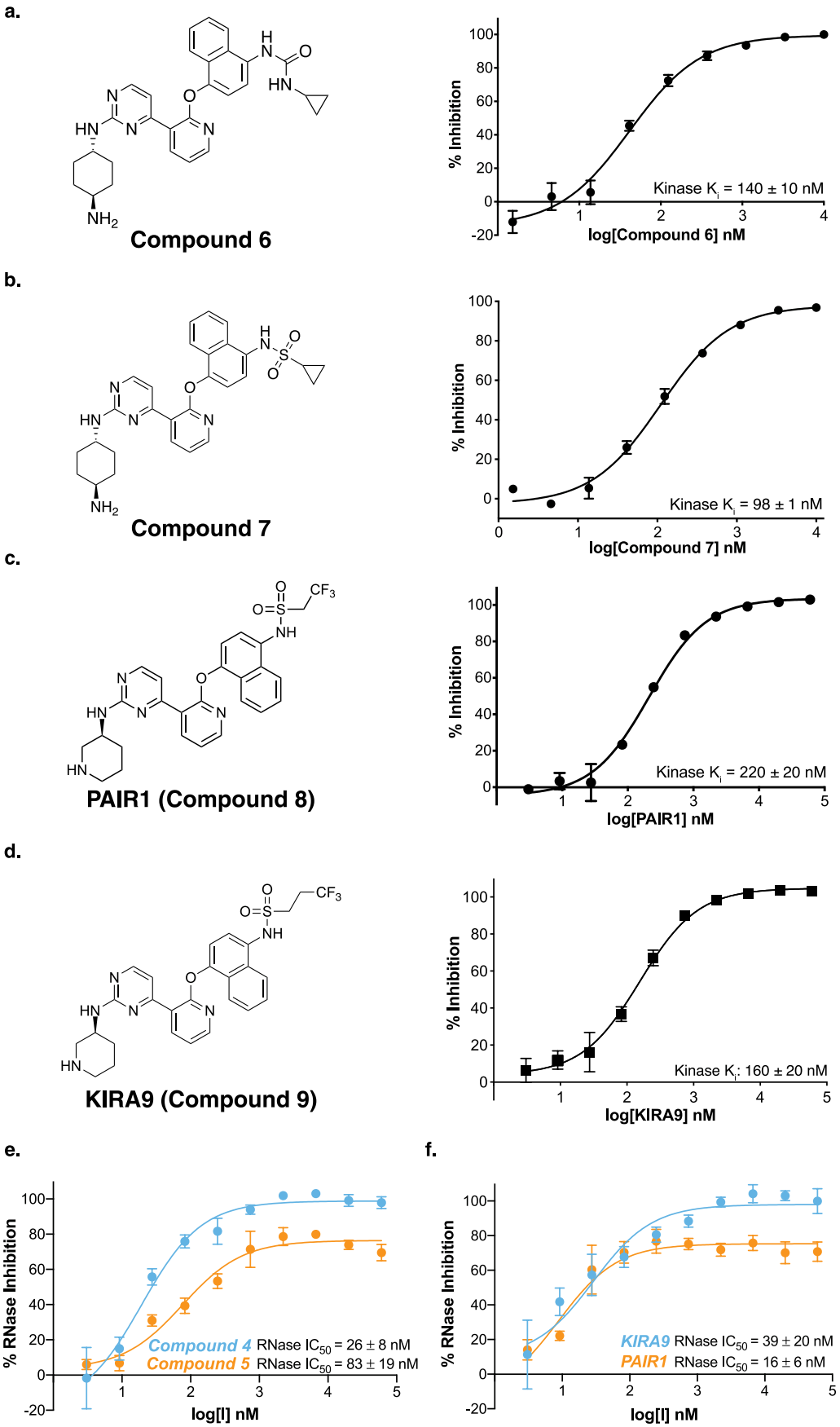

Extended Data Fig. 3 | See next page for caption.

Extended Data Fig. 3 | Structurally-related PAIRs and KIRAs. (**a**) Chemical structure of (*left*) and inhibition of IRE1α*'s kinase activity (*right*, $K_i = 140$ nM) by compound **6**. (**b**) Chemical structure of (*left*) and inhibition of IRE1α*'s kinase activity (*right*, $K_i = 98$ nM) by compound **7**. (**c**) Chemical structure of (*left*) and inhibition of IRE1α*'s kinase activity (*right*, $K_i = 220$ nM) by compound **8** (PAIR1). (**d**) Chemical structure of (*left*) and inhibition of IRE1α*'s kinase activity (*right*, $K_i = 160$ nM) by compound **9** (KIRA9). Inhibition of IRE1α*'s RNase activity by (**e**) compounds **4** and **5**, and **(f)** PAIR1 and KIRA9. All data points shown are the mean of n = 3 independent experiments ± SEM.

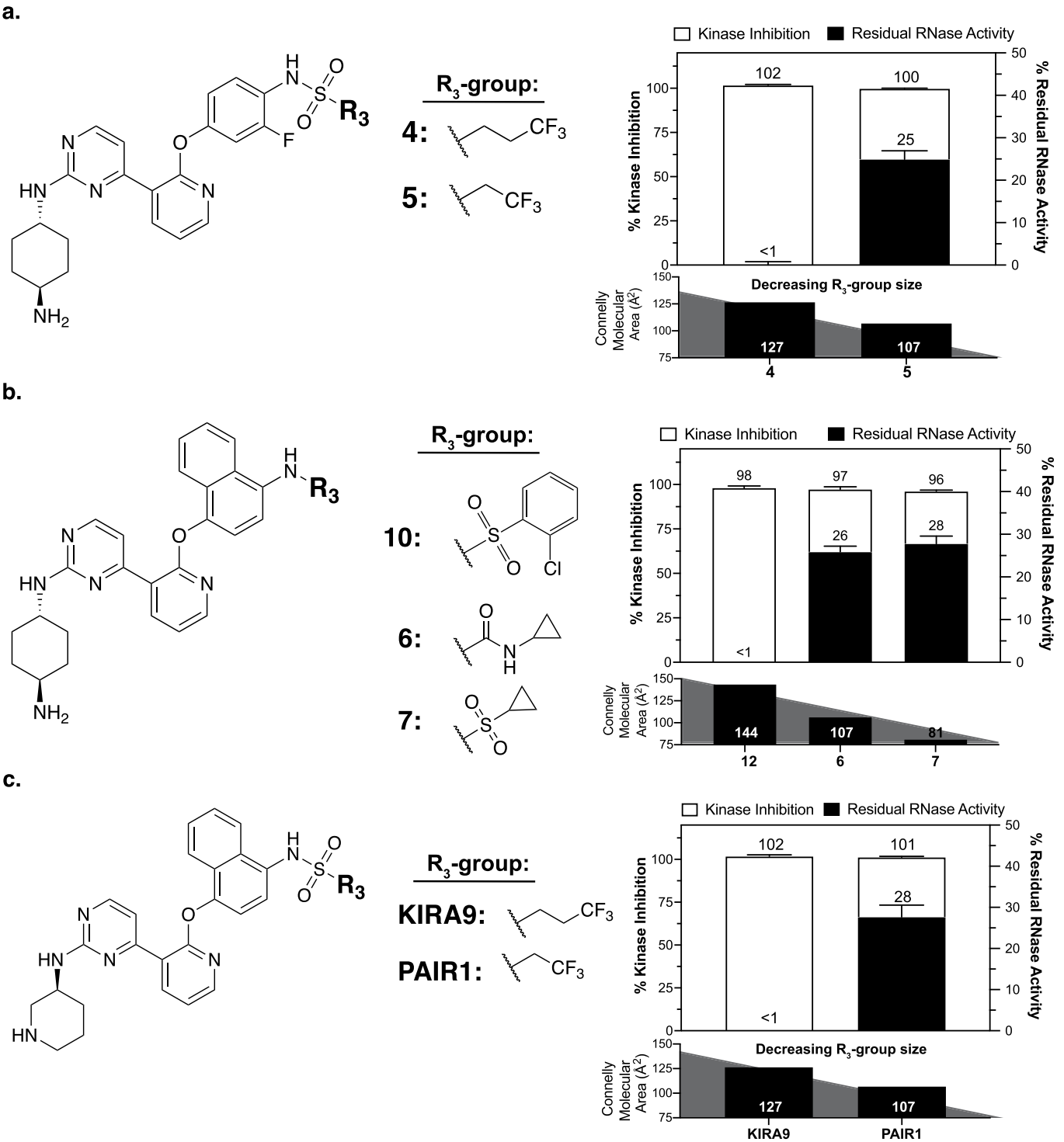

Extended Data Fig. 4 | Partial antagonism of RNase activity is directly related to R³-group size. Three-way correlation of kinase inhibition (a proxy for ATP-binding site occupancy), residual RNase activity, and R³-group size measured as Connolly molecular surface area (Å²) from matched inhibitor sets: (**a**) **4** and **5**, (**b**) **10** (a previously described KIRA), **6**, **7**, and (**c**) KIRA9 and PAIR1. Kinase inhibition and residual RNase activity are shown as the mean of n = 3 independent experiments ± SEM. Note: values are also shown in Fig. 2f.

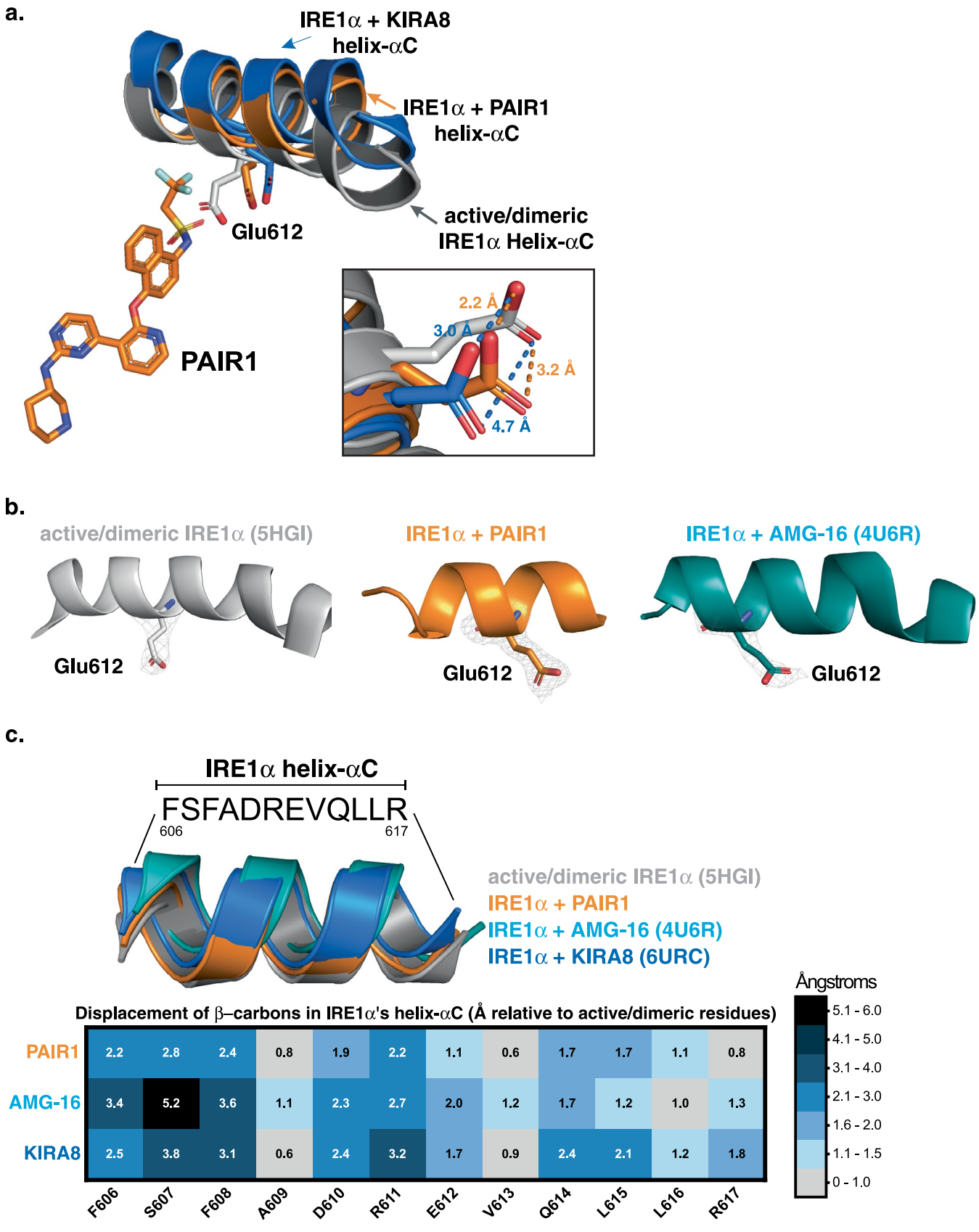

Extended Data Fig. 5 | See next page for caption.

Extended Data Fig. 5 | PAIR1 stabilizes an intermediately displaced helix-αC. (**a**) Superimposition of the helix-αCs of active IRE1α* (*gray*, PDB: 5HGI) with the PAIR1-IRE1α* complex (*orange*), and the KIRA8-IRE1α* complex (*blue*, PDB: 6URC). Inset displays the displacement of Glu612 within the helix-αC relative to active IRE1α* (*gray*, PDB: 5HGI). (**b**) 2Fo-Fc electron density maps of Glu612 from active IRE1α* (*gray*, PDB: 5HGI), PAIR1-IRE1α* (*orange*), and AMG-16-IRE1α* (*teal*, PDB: 4U6R), contoured to 1.0σ shown as gray isomesh, revealing strong electron density for Glu612, making it a suitable residue to measure approximate helix-αC movement. (**c**) Displacement of β-carbons from helix-αC residues (606-617) from co-crystal structures of IRE1α* with PAIR1 (orange), AMG-16 (teal, PDB: 4U6R), and KIRA8 (blue, PDB: 6URC) relative to active IRE1α* (*gray*, PDB: 5HGI).

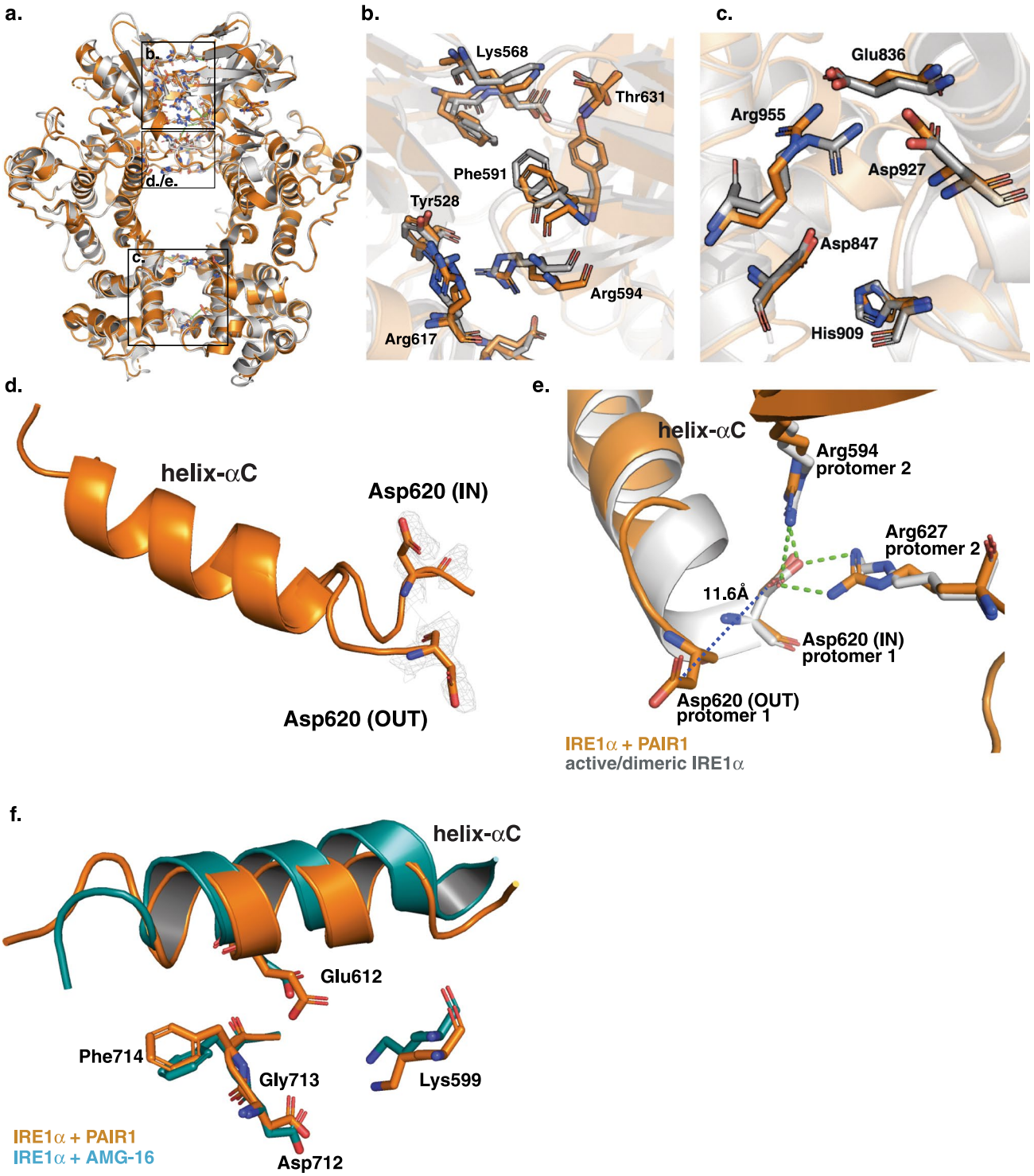

Extended Data Fig. 6 | The PAIR1-bound IRE1α* dimer interface is partially disrupted through Asp 620 displacement. (**a**) Superimposition of the active IRE1α* (*gray*, PDB: 5HGI) and PAIR1-IRE1α* complex (*orange*) dimers. (**b,c**) Zoom-in views of the dimer interface contacts that are similar between active IRE1α* (*gray*, PDB: 5HGI) and the PAIR1-IRE1α* complex (*orange*) dimers. (**d**) 2Fo-Fc electron density maps of Asp620, contoured to 1.0σ shown as gray isomesh, reveal equal distribution of Asp620 between 'in' and 'out' conformations. (**e**) Superimposition of dimer interface residue Asp620 from active IRE1α* (*gray*, PDB: 5HGI) and the PAIR1-IRE1α* complex (*orange*) shows that Asp620-IN is in a similar conformation as active IRE1α* and forms a salt bridge with the side-chains of Arg594 and Arg627 of the adjacent IRE1α* protomer. In the other conformation, Asp620-OUT, the side-chain of Asp620 is displaced 11.6 Å and can no longer form a salt bridge with Arg594 and Arg627. This inter-dimer salt bridge between Asp620 and Arg594/Arg627 is essential for RNase active dimer formation and although Asp620 is found equally in conformations productive (Asp620-IN) and unproductive (Asp620-OUT) for RNase active dimer formation, the cumulative effect is partial disruption of the RNase active dimer interface. (**f**) Superimposition of kinase catalytic residues: K599, Glu612, and the DFG-motif (Asp712, Gly713, Phe714) from the PAIR1-IRE1α* complex (*orange*) and the AMG-16-IRE1α* complex (*teal*, PDB:4U6R) reveal that residues outside of the helix-αC (K599 and the DFG-motif) are in similar conformations, suggesting that differences in the pharmacology between PAIRs and KIRAs stems mainly from helix-αC movement.

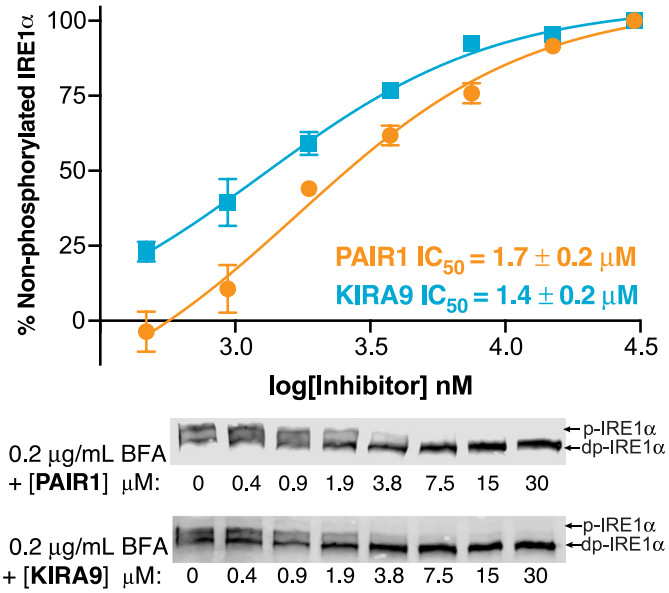

Extended Data Fig. 7 | PAIR1 and KIRA9 equipotently block ER stress-induced IRE1α autophosphorylation. Immunoblots for total IRE1α (*bottom*) from parent INS-1 cells treated with various concentrations of PAIR1 or KIRA9 followed by the addition of 200 ng/μL Brefeldin-A (BFA) for 2 hours. Samples were subjected to phostag SDS-PAGE and % non-phosphorylated IRE1α (*top*) was determined from the ratio of dephosphorylated IRE1α relative to total IRE1α. Values shown are the mean of n = 3 biologically independent samples ± SEM.

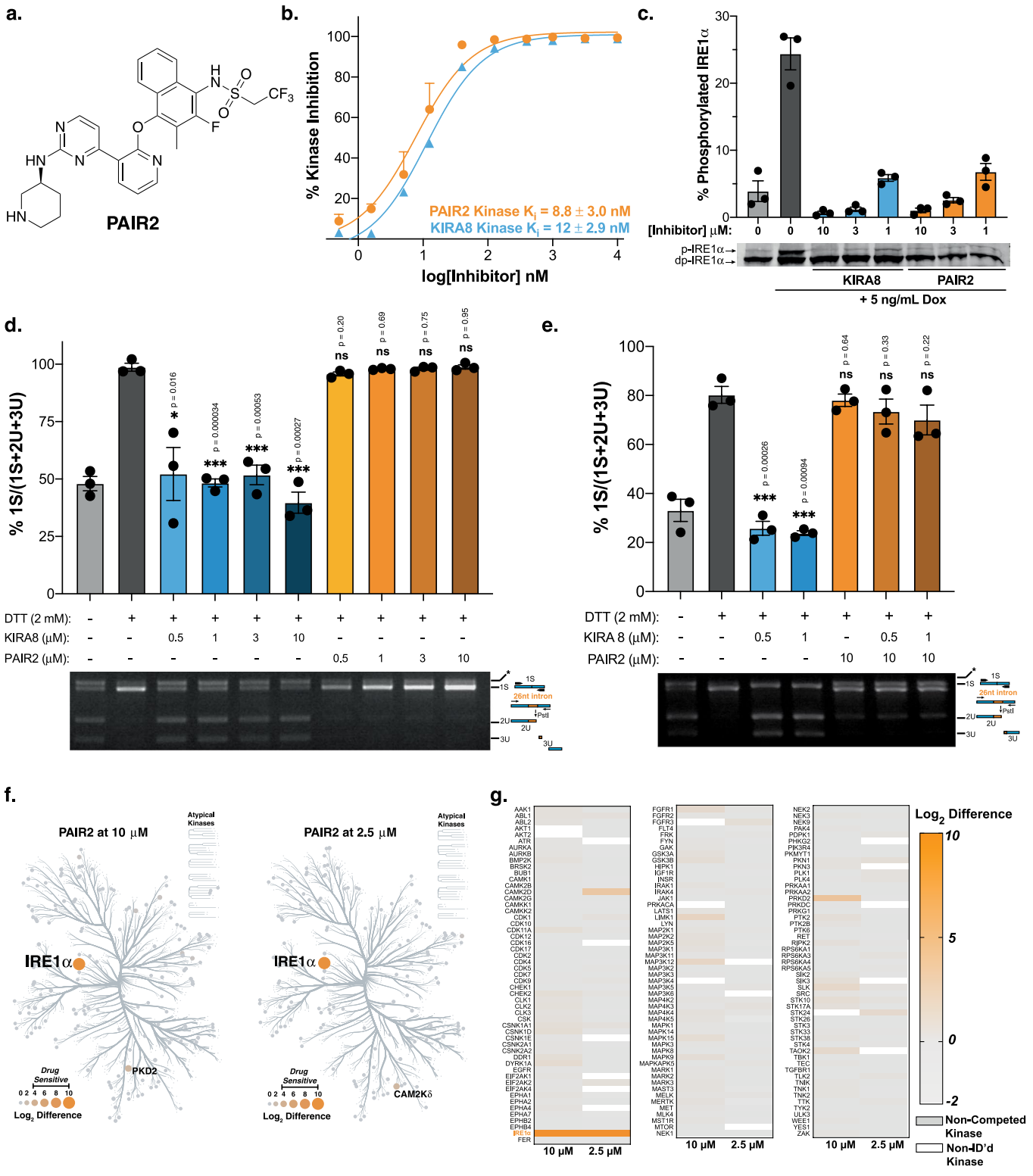

Extended Data Fig. 8 | See next page for caption.

Extended Data Fig. 8 | Characterization of the highly potent PAIR, PAIR2. (**a**) Chemical structure of PAIR2. (**b**) Inhibition of IRE1α*'s kinase activity by PAIR2 (K_i = 8.8 nM, values shown as the mean of n = 3 independent experiments ± SEM) and KIRA8 (K_i = 12 nM, values shown as the mean of n = 2 independent experiments). (**c**) Immunoblots for total IRE1α (*bottom*) from the INS-1 cells described in Fig. 4b treated with various concentrations of PAIR2 or KIRA8 followed by the addition of 5 ng/ml doxycycline (Dox) for 6 hours. Samples were subjected to phostag SDS-PAGE and % phosphorylated IRE1α (*top*) was determined from the ratio of phosphorylated IRE1α relative to total IRE1α. Values shown are the mean of n = 3 independent experiments ± SEM. (**d**) Percent spliced XBP1 (quantified from PstI-digested XBP1 cDNA amplicons) from parent INS-1 cells treated with DMSO, PAIR2, or KIRA8 (0.5, 1, 3, 10 μM) followed by the addition of 2 mM 1,4-dithiothreitol (DTT) (*top*). Data shown are the mean of n = 3 biologically independent samples ± SEM. A representative EtBr-stained agarose gel of XBP1 cDNA amplicons is shown below. (**e**) Percent spliced XBP1 (quantified from PstI-digested XBP1 cDNA amplicons) from parent INS-1 cells treated first with DMSO (lanes 1-4) or 10 μM PAIR2 (lanes 5-7) for 30 minutes followed by treatment with either DMSO (lanes 1, 2, and 5) or 0.5 or 1 μM KIRA8 (lanes 3, 4, 6, and 7) for 30 minutes followed by the addition of 2 mM 1,4-dithiothreitol (DTT) (*top*). Data shown are the mean of n = 3 biologically independent samples ± SEM. A representative EtBr-stained agarose gel of XBP1 cDNA amplicons is shown below. (**f**) Kinome selectivity of PAIR2 as determined by kinobead profiling. Kinases that were identified in the profiling experiment are shown with gray circles. Circle size and color have been scaled to the $\log_2$ ratio (difference in LFQ intensity) between DMSO and treatment with 10 and 2.5 μM of PAIR2 (mean of three and four replicates, respectively). Kinases reported as being drug-sensitive (Log_2 Difference > 2) were also required to show significance from a two-sample T-test with FDR of 0.05. (**g**) Heat map displaying kinome selectivity from (f). P values calculated in (d), (e) are versus DTT treated cells and were determined using a two-tailed Student's t-test. *P < 0.05, **P < 0.01, ***P < 0.001.

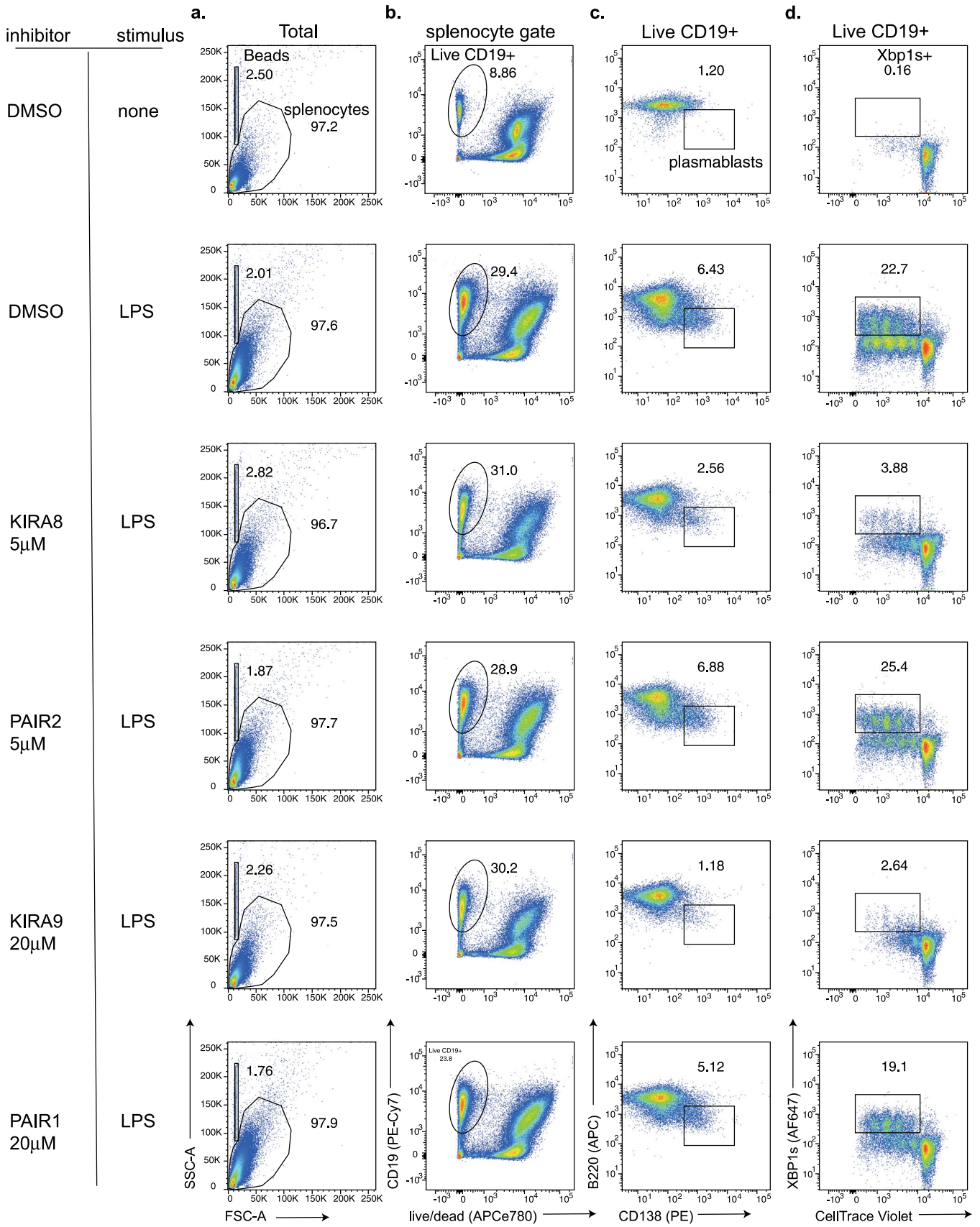

Extended Data Fig. 9 | See next page for caption.

Extended Data Fig. 9 | Flow cytometric analysis of lipopolysaccharide (LPS)-treated mouse splenocytes. Mouse splenocytes were loaded with vital dye and subsequently cultured +/− 1 μg/mL LPS for three days in the presence or absence of KIRA8, KIRA9, PAIR1, or PAIR2 at noted concentrations. Following culture, cells were stained to detect surface marker expression and subsequently permeabilized to detect XBP1s intracellular expression. Samples were mixed with a fixed number of counting beads and collected by flow cytometry. Representative plots are displayed. **(a)** Splenocytes and beads were first gated on the basis of forward scatter (FSC) and side scatter (SSC) for the purpose of absolute quantification of cell number. (**b**) Live B-cells were then identified on the basis of CD19 expression and exclusion of live/dead dye. (**c**) Plasmablasts were identified as CD19+ cells with downregulation of B220 and upregulation of CD138 expression. **(d)** Plots depict vital dye dilution as a marker of cell division and XBP1s + gate. Corresponding quantification of these cell populations is shown in Fig. 6 and Extended Data Fig. 10.

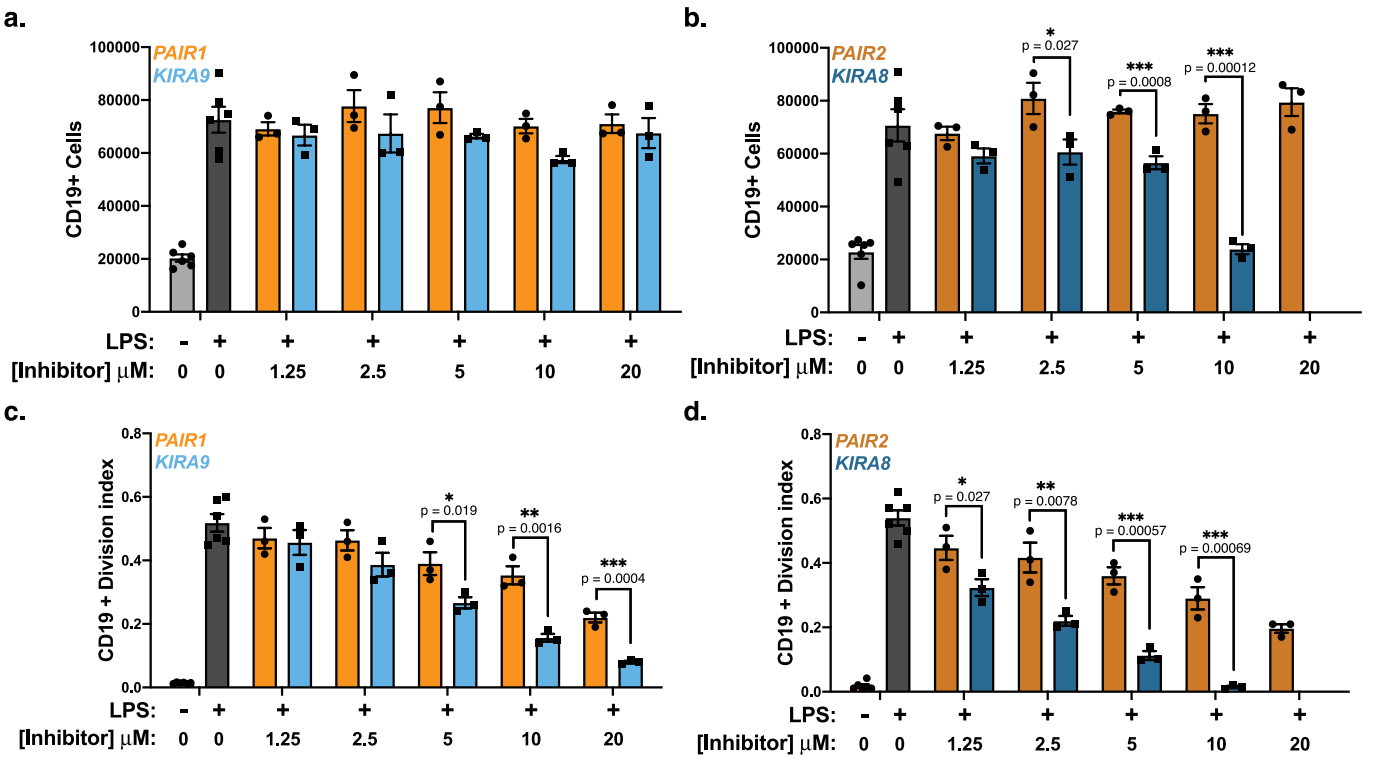

Extended Data Fig. 10 | Effect of PAIRs and KIRAs on B-cell division. Quantification of CD19 positive cells following treatment of mouse splenocytes with 1 μg/mL LPS for three days in the presence or absence of various concentrations of (**a**) PAIR1 (*orange*) or KIRA9 (*teal*) or (**b**) PAIR2 *(dark orange)* or KIRA8 *(dark blue)* as gated in Extended Data Fig. 9. (**c, d**) Division index of CD19 + cells treated as in (a, b) was calculated via Flowjo on the basis of vital dye dilution (as shown in Extended Data Fig. 9). P values were calculated using one-tailed Student's t-test. *P < 0.033, **P < 0.002, ***P < 0.001. Data for 20 μM KIRA8 could not be generated due to cellular toxicity. All data shown are the mean of n = 3 biologically independent samples ± SEM.